Check for updates

X-ray-activated persistent luminescence nanomaterials for NIR-II imaging

Peng Pei[1], Ying Chen[1], Caixia Sun[1], Yong Fan [1 ✉], Yanmin Yang[2 ✉], Xuan Liu[1], Lingfei Lu[1], Mengyao Zhao[1], Hongxin Zhang[1], Dongyuan Zhao [1], Xiaogang Liu [3,4] and Fan Zhang [1 ✉]

Persistent luminescence is not affected by background autofluorescence, and thus holds the promise of high-contrast bioimaging. However, at present, persistent luminescent materials for in vivo imaging are mainly bulk crystals characterized by a non-uniform size and morphology, inaccessible core–shell structures and short emission wavelengths. Here we report a series of X-ray-activated, lanthanide-doped nanoparticles with an extended emission lifetime in the second near-infrared window (NIR-II, 1,000–1,700 nm). Core–shell engineering enables a tunable NIR-II persistent luminescence, which outperforms NIR-II fluorescence in signal-to-noise ratios and the accuracy of in vivo multiplexed encoding and multilevel encryption, as well as in resolving mouse abdominal vessels, tumours and ureters in deep tissue (~2–4 mm), with up to fourfold higher signal-to-noise ratios and a threefold greater sharpness. These rationally designed nanoparticles also allow the high-contrast multiplexed imaging of viscera and multimodal NIR-II persistent luminescence–magnetic resonance–positron emission tomography imaging of murine tumours.

Optical imaging in the second near-infrared (NIR-II, 1,000–1,700 nm) window with low tissue scattering has great utility in biological and medical sciences due to its high sensitivity and high spatiotemporal resolutions[1–5]. Recently, a clinical study also highlighted the promising clinical potential of intraoperative NIR-II fluorescence (FL) imaging and NIR-II image-guided surgery[2]. However, limitations still exist due to the tissue autofluorescence background that results from the inevitable, real-time excitation light (Supplementary Fig. 1)[1,6,7], which compromises the imaging quality and specificity in living tissues, as well as to the potential light-induced overheating and inhomogeneous illumination in wide-field imaging[7–10].

Persistent luminescence (PL) is a distinct optical phenomenon and can last for minutes or even several hours after excitation ceases[11–13]. For this reason, it has promise for applications in in vivo bioimaging and biosensing[14–23], as well as in in vivo security encryption and information storage[24]. Nevertheless, the current generation of PL materials are mainly large crystals, grown using synthetic methods that involve solid-state annealing at extremely high temperatures (>1,000 °C) (refs [19–21,25–27]), that lack nanostructure modulation and surface property tunability. These drawbacks are compounded by emissions in the visible (400–700 nm) (refs [19,21]) and first near-infrared (NIR-I, 700–900 nm) (refs [27]) windows, which hamper high-contrast imaging in deep tissue[19–21,25–27]. On the other hand, these materials generally require ultraviolet[20,21,26,27] or visible[19,25] light to charge, which limits their energy enrichment, especially in the presence of tissue scattering and absorption. By contrast, high-energy X-rays, which have been employed in radiotherapy and bioimaging[28], can activate materials with large bandgaps (Extended Data Fig. 1) and stimulate PL, but the emissions are still limited to the ultraviolet and visible windows[29–32]. To date, the development of X-ray-activated, nanosized PL materials with a tunable luminescence in the NIR-II window, as

well as a well-controlled, multifunctional nanostructure for in vivo imaging, constitutes a notable challenge and remains unexplored (Supplementary Table 1).

Here we report the synthesis of X-ray-activated, lanthanide-doped PL nanoparticles (Ln-PLNPs) that can address the aforementioned drawbacks. A series of Ln-PLNPs that offer NIR-II PL emission for more than 72 hours was developed by tailoring the activator composition. We first investigated the influence of structural parameters and the temperature of Ln-PLNPs on their PL intensity, and proposed a plausible mechanism of X-ray-activated Ln-PLNPs. By engineering the core–shell structure in single nanoparticles, we demonstrated tunable NIR-II PL with a high-capacity encoding and robust decoding feasibility in deep tissue. Finally, we evaluated the optical performance of Ln-PLNPs in several in vivo imaging applications, which included high-contrast abdominal vessels, tumour imaging and ureter tracking, as well as multispectral in vivo deep-tissue viscera imaging and the multimodal PL–magnetic resonance–positron emission tomography (PET) imaging of tumours.

X-ray-activated Ln-PLNPs with a tunable emission

Ln-PLNPs with a core–shell structure were synthesized via the hot-injection solution method by introducing low-phonon energy $NaY(Gd)F_4$ as the host material[33–35] and various rare-earth dopants (for example, Nd^{3+}, Ho^{3+}, Tm^{3+} or Er^{3+}) as the activators (Fig. 1a). High-resolution scanning transmission electron microscopy images revealed the uniform morphology of the as-synthesized Ln-PLNPs with a hexagonal phase (Fig. 1b), which was also confirmed by X-ray diffraction (Supplementary Fig. 2a). The emission properties of the Ln-PLNPs were first investigated by X-ray irradiation (FL spectra), which yielded narrow and tunable emissions in the visible and NIR-I windows, as well as in the NIR-II window (1,064 nm for Nd^{3+}, 1,180 nm for Ho^{3+}, 1,475 nm for Tm^{3+} and 1,525 nm for Er^{3+}) (Supplementary Fig. 3). After stopping the X-ray irradiation,

[1]Department of Chemistry, State Key Laboratory of Molecular Engineering of Polymers and iChem, Shanghai Key Laboratory of Molecular Catalysis and Innovative Materials, Fudan University, Shanghai, China. [2]College of Physics Science and Technology, Hebei University, Baoding, China. [3]Department of Chemistry, National University of Singapore, Singapore, Singapore. [4]Joint School of National University of Singapore and Tianjin University, International Campus of Tianjin University, Fuzhou, China. ✉e-mail: fan_yong@fudan.edu.cn; mihuyym@163.com; zhang_fan@fudan.edu.cn
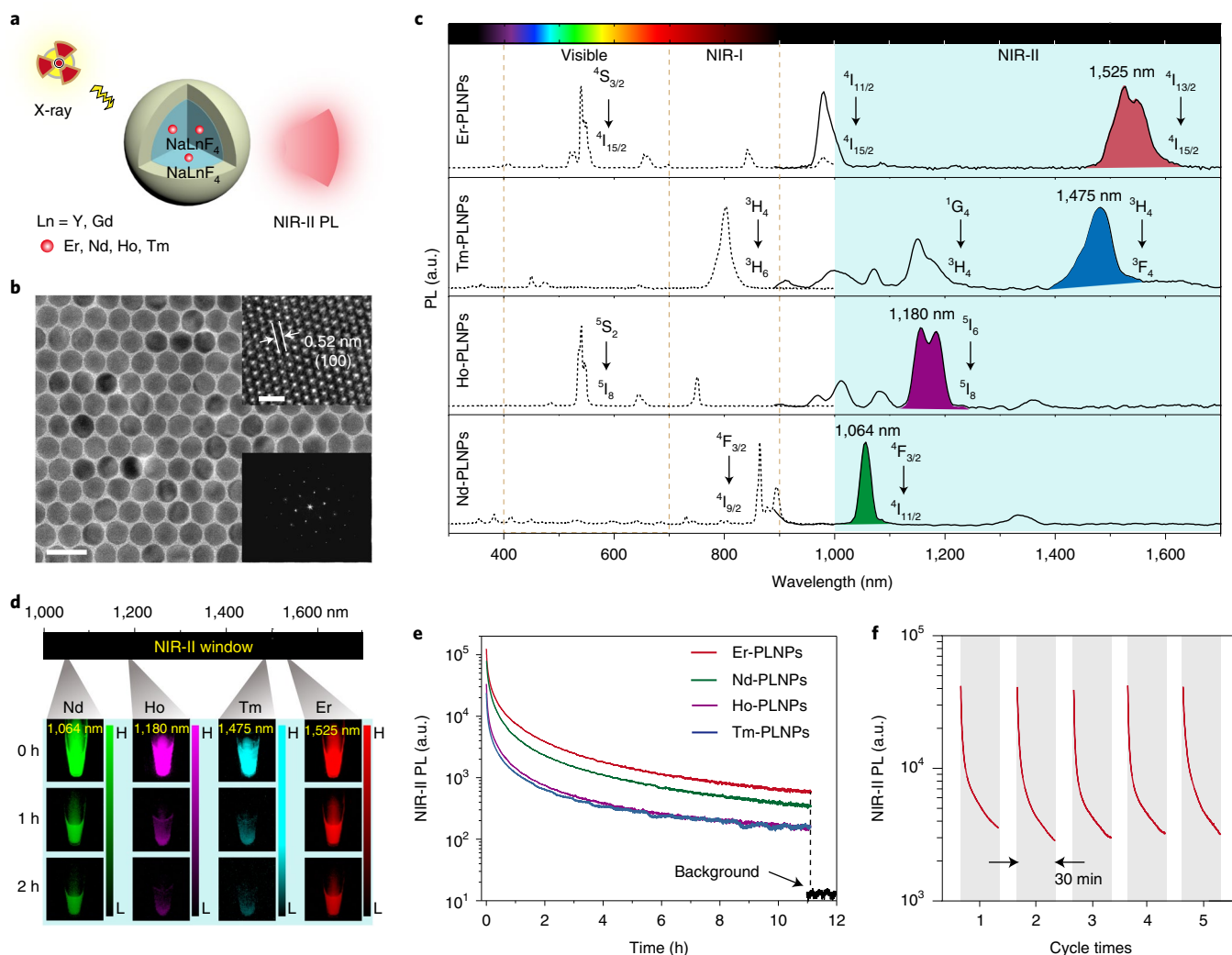
Fig. 1 | X-ray-activated PL from Ln-PLNPs. a, Schematic representation of X-ray-activated PL generated in lanthanide-doped nanoparticles. **b**, Low-resolution transmission electron microscopy (TEM) image of the as-synthesized NaYF$_4$:3%Er@NaYF$_4$ nanoparticles. Scale bar, 50 nm. Insets: a high-resolution TEM image of a single NaYF$_4$:3%Er@NaYF$_4$ nanoparticle (top right) and the corresponding electron diffraction pattern (bottom right). Scale bar, 2 nm. **c**, Tunable PL spectra of Ln-PLNPs after X-ray irradiation. **d**, NIR-II PL images of Nd-, Ho-, Tm- and Er-PLNPs in centrifuge tubes as a function of time. H, high; L, low. **e,f**, PL decay curves of typical emission bands of Ln-PLNPs (**e**) and NIR-II PL photostability of Er-PLNPs (**f**) in the NIR-II window derived from NIR-II PL images. Imaging exposure time, 5 s. a.u., arbitrary units.

the emission patterns of Ln-PLNPs, the same as those in their FL spectra, continued (Fig. 1c). PL in the NIR-II window lasted more than 72 hours (Fig. 1d,e, Extended Data Fig. 2 and Supplementary Table 2). The initial intensity of the PL showed a positive correlation with X-ray dosage and reached a plateau when higher dosages of X-rays (>200 Gy) were used (Supplementary Fig. 4). This phenomenon is probably due to a limitation in the harvesting of the excitation energy by the nanoparticles. Moreover, these Ln-PLNPs showed a high photostability. No noticeable change in the morphology or crystal structure was observed after five cycles of X-ray recharging (Fig. 1f, Supplementary Fig. 2 and Supplementary Table 2).

Optical property optimization of NIR-II Ln-PLNPs

Structural parameters, which include the dopant concentration, core size, shell thickness, crystalline phase and host matrix, are important determinants of the optical properties of Ln-PLNPs. For example, for core–shell-structured Er-doped PLNPs (Er-PLNPs, such as NaYF$_4$:Er@NaYF$_4$) (Supplementary Figs. 5 and 6), the optimal doping concentration of Er^{3+} was set at 3% by recording the PL

intensity at 1,525 nm (Fig. 2a and Supplementary Fig. 7a). Further elevating the doping concentration quenched the PL due to deleterious cross-relaxation. In addition, Er-PLNPs with larger cores and thicker shells showed an enhanced PL because of the effective isolation of the activators from surface quenchers (Fig. 2b,c). Optimal Er-PLNPs with 35 nm cores and 7 nm shells showed an approximately 25-fold enhancement in PL intensity, compared with that of the as-prepared 22 nm core nanoparticles (Fig. 2c). Further increasing the core size or shell thickness yielded little improvement in the PL intensity. The PL intensity of Er-PLNPs in the hexagonal phase was more than ten times stronger than that in the cubic-phase counterparts (Extended Data Fig. 3), which was ascribed to a decreased level of crystal defects or internal quenching in the hexagonal-phase fluorides[36]. Similar results were also observed for Ln-PLNPs doped with Nd^{3+}, Ho^{3+} or Tm^{3+} activators by optimizing their PL emissions in the NIR-II window (Supplementary Figs. 8–10).

The PL intensities of the Ln-PLNPs were also affected by the host matrix. We first replaced Y^{3+} with different ratios of Gd^{3+} in NaYF$_4$:3%Er@NaYF$_4$ PLNPs during synthesis. By increasing the
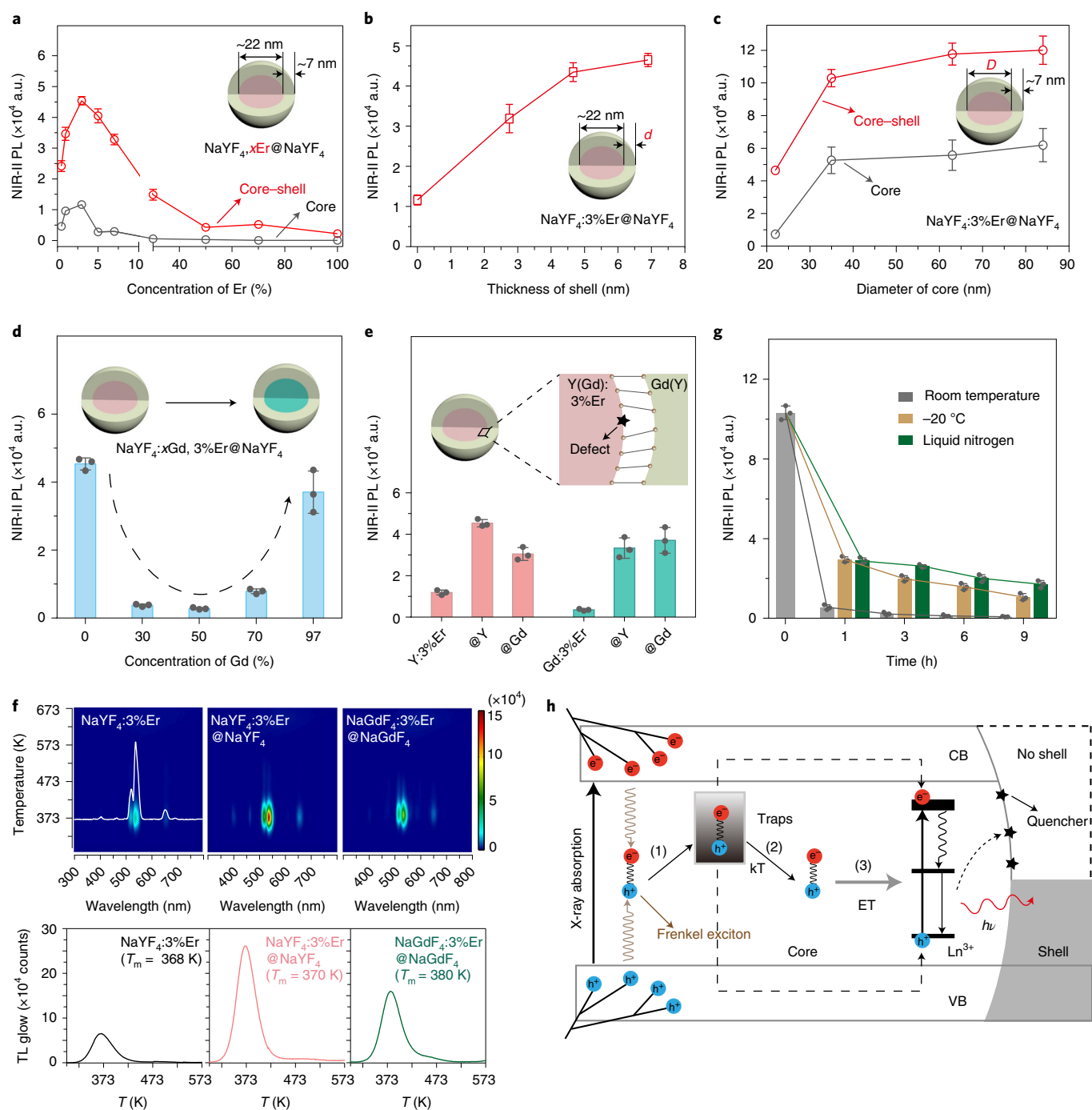
Fig. 2 | Controlled structures and compositions of Ln-PLNPs for NIR-II PL investigation. a–d, Influence of activator concentration (**a**), shell thickness (*d*) (**b**), core diameter (*D*) (**c**) and host materials (**d**) on the NIR-II PL intensity of Er-PLNPs. **e**, Influence of interfacial defects between the core and shell on the NIR-II PL intensity of Er-PLNPs. Y:3%Er, @Y and @Gd for pink histograms represent $NaYF_4$:3%Er, $NaYF_4$:3%Er@$NaYF_4$ and $NaYF_4$:3%Er@$NaGdF_4$, respectively. Gd:3%Er, @Y and @Gd for green histograms represent $NaGdF_4$:3%Er, $NaGdF_4$:3%Er@$NaYF_4$ and $NaGdF_4$:3%Er@$NaGdF_4$, respectively. **f**, Contour maps of TL intensity as a function of emission wavelength and temperature for Er-PLNPs with different host materials (overlay of the TL spectrum at 368 K is shown in the top-left panel) and the corresponding TL glow curves derived from the integral intensity of contour maps. **g**, Influence of storage temperature on the NIR-II PL intensity of Er-PLNPs. Pre-irradiated samples were stored at low temperatures and quickly recovered to room temperature before their PL signals were acquired. Imaging exposure time, 5 s. *n* = 3 independent experiments. **h**, Proposed mechanism of X-ray-activated PL, showing the formation of excitons, PL (process (1), process (2) and process (3)), and the shell influence. e⁻, electrons; h, holes; *k*, Boltzmann's constant; *T*, temperature; ET, energy transfer; CB, conduction band; VB, valence band; black stars, quenchers on the core surface. The data are shown as the mean ± s.d.

amount of Gd^{3+}, the PL intensity of Er-PLNPs first decreased and then increased. This PL intensity valley was obtained with co-doped $NaYF_4$:50%Gd, which was 12 times lower than that of pure $NaGdF_4$ or $NaYF_4$ hosts (Fig. 2d). This phenomenon can be attributed to

increased lattice defects that result from the atomic size mismatch between Gd^{3+} and Y^{3+}. In addition, for core–shell PLNPs, a more efficient PL was observed with the same host material in the core and shell, due to the well-matched lattice interface, as demonstrated

in the cases of NaYF$_4$:3%Er@NaYF$_4$ or NaGdF$_4$:3%Er@NaGdF$_4$ nanoparticles (Fig. 2e and Supplementary Figs. 7b,11). In comparison, a NaGdF$_4$ host has deeper energy traps than a NaYF$_4$ matrix, as validated by thermoluminescence (TL) results in which a higher conduction band edge was calculated for NaGdF$_4$:3%Er@NaGdF$_4$ (0.76 eV at 380 K) than that for NaYF$_4$:3%Er@NaYF$_4$ (0.74 eV at 370 K) based on the Urbach equation[37] (Fig. 2f). This property can explain the lower PL intensity of Er-PLNPs with a NaGdF$_4$ host than that with a NaYF$_4$ host (Fig. 2e). TL results also reveal that an inert shell exerts no influence on the depth of energy traps, as indicated by the identical peak positions of TL glow for core–shell NaY(Gd)F$_4$:3%Er@NaY(Gd)F$_4$ and NaY(Gd)F$_4$:3%Er core nanoparticles (Fig. 2f and Supplementary Fig. 12). This was further verified in Ln-PLNPs doped with Nd^{3+}, Ho^{3+} and Tm^{3+} activators (Supplementary Fig. 13).

Apart from the nanoparticle structural parameters, low-temperature storage was implemented to slowly release the stored energy, which led to a much enhanced PL intensity in the NIR-II window (>12 fold at six hours) than that at room temperature (Fig. 2g). Storage at −20 °C can extend the persistence over 45 days (Extended Data Fig. 4).

Based on the above analysis, we propose a plausible mechanism for X-ray-activated NIR-II PL (Fig. 2h). On X-ray irradiation, excited electrons enter the conduction band of fluoride materials through photoelectric ionization, the Auger effect and energy collision[38–40] to create electron–hole pairs (Frenkel excitons). These stable free excitons can be transferred in the host matrix and captured by energy traps, which are probably fluoride vacancies and fluoride Frenkel defects (vacancy–interstitial pairs) formed due to a thermal dissociation during the material synthesis and X-ray irradiation[11,32]. The high bandgap and confinement effect of the nanosized fluoride[41–45] mean that the captured free excitons form bounded excitons. They are slowly released as free excitons again due to thermal perturbation and subsequently captured by the activators (Nd^{3+}, Ho^{3+}, Tm^{3+} or Er^{3+}). Electrons and holes escape to the conduction band and valence bands, respectively, and then they migrate towards the activators. The captured electron–hole pairs recombine to transfer energy to activators to generate PL. The entire NIR-II PL process is dominated by a large bandgap, finely adjusted architecture and fluoride host materials. These factors can greatly enhance energy storage and suppress deleterious non-radiative energy transition, and thus improve the PL efficiency. Exploiting this mechanism, PL from this high-bandgap host material (NaYF$_4$) doped with other rare earths (for example, Yb^{3+}, Pr^{3+}, Tb^{3+}, Dy^{3+} and Sm^{3+}) was also realized (Extended Data Fig. 5).

Ln-PLNPs for multiplexed encoding and encryption

Compared with conventional bulk PL materials, Ln-PLNPs with controllable core–shell structures offer superior optical properties, as they can adapt to emit bright and precisely tunable emission in the NIR-II window. As a proof of concept, we synthesized NaYF$_4$:1%Ho@NaGdF$_4$@NaYF$_4$:3%Er@NaGdF$_4$@NaYF$_4$:1%Nd@ NaGdF$_4$ multilayered Ho/Er/Nd-PLNPs (Fig. 3a,b and Extended Data Fig. 6). Elimination of the cross-relaxation between different activators led to bright NIR-II PLs in the Ho, Er and Nd emission channels simultaneously in multilayered Ho/Er/Nd-PLNPs, which were 13-, 16- and 14-fold more intense than that in the Ho/Er/Nd-co-doped control (NaYF$_4$:1%Ho,3%Er,1%Nd@NaGdF$_4$) (Fig. 3a,c,d and Extended Data Fig. 6). These independently engineered NIR-II PL signals enabled the NIR-II PL encoding of different carriers, and so delivered a high multiplexing level with higher signal-to-noise ratios (SNRs) and accuracy than those of conventional NIR-II FL imaging. To this end, polydimethylsiloxane (PDMS) beads with a series of encapsulated multilayered PLNPs were randomly mixed and placed in a Petri dish covered with 2 mm mimic tissue (1% Intralipid) (Fig. 3e and Supplementary Fig. 14).

NIR-II PL and NIR-II FL imaging (808 nm excitation) were performed for the three emission bands of PDMS codes. Although the NIR-II PL intensity decreased over time, NIR-II PL images showed higher SNRs (>3-fold in the Er channel and >30-fold in the Nd channel) and sharper full-width at half-maxima (FWHM, <0.83-fold in the Er channel and <0.68-fold in the Nd channel) than the corresponding NIR-II FL images (Fig. 3f,g and Supplementary Fig. 15). This could be ascribed to the elimination of scattered signals from excitation. The encoding beads were unambiguously decoded in deep tissues using high-contrast NIR-II PL images (Fig. 3e and Supplementary Table 3). By contrast, the decoding process of conventional NIR-II FL images was challenging because of the low SNR in the shorter emission band (1,064 nm for Nd^{3+}) or the missing signal (1,180 nm for Ho^{3+}) under an 808 nm excitation (Fig. 3e and Supplementary Fig. 16).

We also found that the ratios of the NIR-II PL signals from different emission bands of multilayered Ln-PLNPs were constant over time (>60 minutes) and independent of their concentrations and temperature (Extended Data Fig. 7). This feature offers a stable ratiometric PL that can be utilized for in vivo multiplexed encoding and multilevel encryption. We demonstrated the construction of a library of optical codes with varied PL ratios, which spanned two orders of magnitude (from 0.32 to 15.82), and with a low coefficient of variation, less than 10%, by carefully adjusting the thickness of the activation layer and activator compositions in multilayered nanoparticles (Fig. 3h,i, Supplementary Figs. 17–19 and Supplementary Table 4; the largest ratio of 15.82 is not included for a better visual effect). Inspired by ratio-tunable PL signals in multilayered Ln-PLNPs, we developed a flexible PDMS butterfly pattern by casting the multilayered Ho/Er-PLNPs onto a glass substrate for multiplexed encoding and decoding applications (Fig. 3j). Steady ratiometric signals from different windows remained constant over time with typical decay characteristics of PL for both the Ho and Er channels displayed. This simultaneous, dynamic, steady luminescence can boost coding capacity and encryption level.

High-contrast in vivo PL imaging with Ln-PLNPs

Ln-PLNPs with a PL emission in the NIR-II window are ideal for in vivo high-contrast imaging and their suitability for biological applications was verified by their stability and biocompatibility in biological media (Extended Data Fig. 8 and Supplementary Figs. 20–22). We then explored Er-PLNPs for in vivo high-contrast and high-resolution vascular and tumour imaging in live mice. Pre-irradiated Er-PLNPs were stored at −20 °C for 0.5 h, and then warmed to room temperature before being injected into a live mouse via an abdominal vein (Fig. 4a and Supplementary Fig. 23). At 10 s postinjection (p.i.), the abdominal vascular network (imaging depth ~1–2 mm) with many tiny capillary vessels branching from larger vessels was clearly delineated by NIR-II PL and NIR-II FL signals. A cross-sectional intensity profile of two of the vessels showed a Gaussian-fitted FWHM of 331.1 μm (position 1) and 457.4 μm (position 2) by NIR-II PL imaging, which were 0.83-fold sharper than those obtained with NIR-II FL imaging (Fig. 4b). Despite the decay of NIR-II PL over five minutes in live mice, the FWHM of NIR-II PL images was still sharper than the NIR-II FL images (Supplementary Fig. 23). Therefore, vascular mapping with a high spatial resolution in living mice can be achieved using Er-PLNPs with NIR-II PL.

NIR-II PL was also tested and compared with NIR-II FL for the imaging of tumours in living mice. The hydrophilic Er-PLNPs were injected into 4T1 tumour-bearing mice via an abdominal vein, and then both the NIR-II PL and NIR-II FL signals were acquired in real time (Fig. 4c and Supplementary Fig. 24). Despite the inevitable PL decay, the tumour site can still be highlighted by the NIR-II PL signal with a high tumour-to-normal tissue (T/N) ratio of 40.9 at 5 min p.i., owing to long-lasting PL and reduced background noise
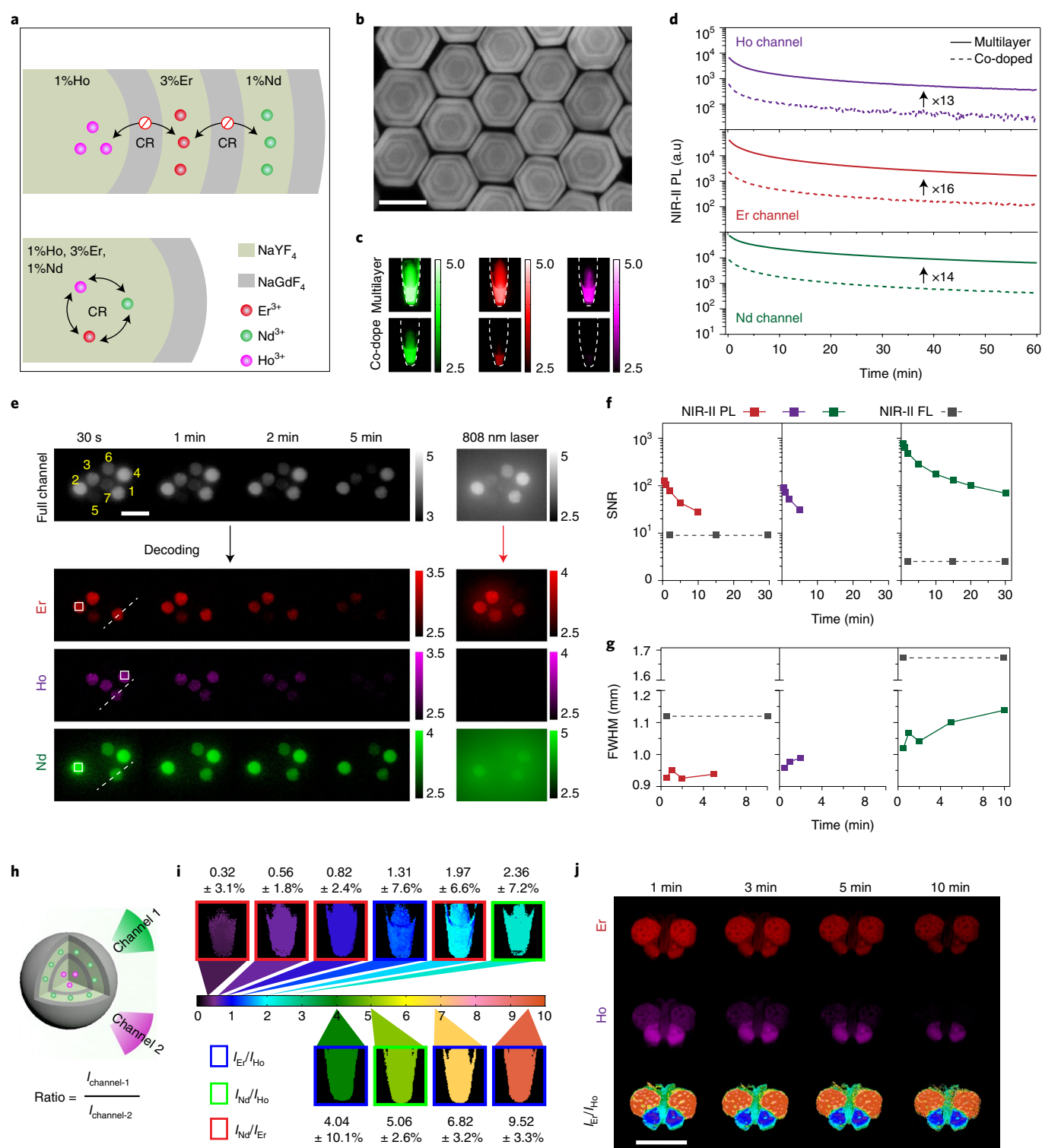
Fig. 3 | NIR-II PL multiplexed encoding with multilayered PLNPs. a, Schematic design of Ln-PLNPs with multilayered (top) and co-doped (bottom) configurations. CR, cross-relaxation. **b**, High-angle annular dark-field–scanning transmission electron microscopy of the multilayered Er/Nd/Ho-PLNPs in **a**. Scale bar, 50 nm. **c,d**, NIR-II PL images after X-ray irradiation ceases (**c**) and NIR-II PL decay curves (**d**) of the multilayered and co-doped PLNPs in **a** for the Nd (green), Er (red) and Ho (magenta) channels. **e**, PL coding of PDMS beads that encapsulate different multilayered PLNPs. NIR-II PL (left column) and NIR-II FL (right column) images were acquired in all three (Nd^{3+}, Ho^{3+} and Er^{3+}) channels covered with mimic tissue (1% Intralipid) over time. Scale bar, 5 mm. **f,g**, SNR (**f**) and FWHM (**g**) of the PDMS beads in **e** as a function of time for the Er (left), Ho (middle) and Nd (right) channels. **h**, Scheme of ratiometric PL codes using multilayered PLNPs with different activators. *I*, PL intensity. **i**, Pseudocolour-mapped ratiometric PL images of multilayered PLNPs in centrifuge tubes. The numbers that accompany each image indicate mean ± the coefficient of variation of the calculated ratios, taken from pixels that correspond to each tube in the PL images. **j**, NIR-II PL and ratiometric PL images of a PDMS butterfly pattern from multilayered Ho/Er-doped PLNPs ($NaYF_4$:1%Ho@$NaGdF_4$@$NaYF_4$:3%Er@$NaGdF_4$) with different luminescence ratios (forewings, $I_{Ho}/I_{Er} = 9.52$; hindwings, $I_{Ho}/I_{Er} = 1.31$; body, $I_{Ho}/I_{Er} = 4.04$). Scale bar, 5 mm. Imaging exposure time, 10 s.
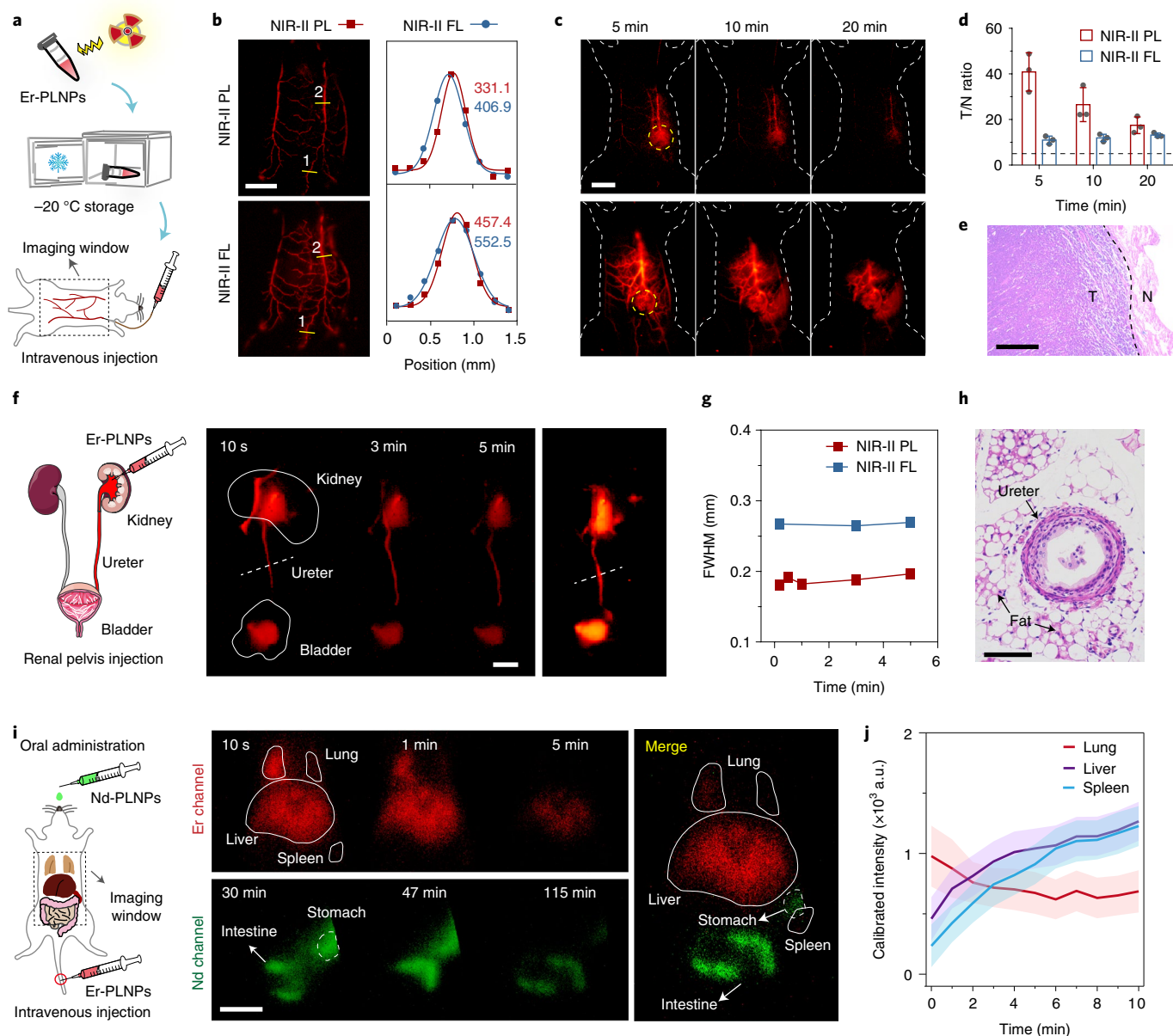
Fig. 4 | X-ray-activated Ln-PLNPs for in vivo high-contrast PL imaging. a, Schematic illustration of NIR-II PL imaging of blood vessels. **b**, NIR-II PL (top left) and NIR-II FL (bottom left) images of blood vessels in a living mouse after intravenous injection of Er-PLNPs at 10 s p.i. (left), and the corresponding normalized intensity profiles of blood vessels (right) at positions 1 (top right) and 2 (bottom right). The FWHMs (μm) are shown. Scale bar, 1 cm. **c**, Time-dependent NIR-II PL (top) and NIR-II FL (bottom) images of tumours on living mice after multiple injections of Er-PLNPs. Scale bar, 1 cm. **d**, T/N ratios of the tumours shown in **c** (n = 3 biologically independent mice). The black dashed line demarcates the Rose criterion. **e**, H&E staining results of the removed tumour. Scale bar, 400 μm. **f**, Time-dependent NIR-II PL (centre) and NIR-II FL (right) images of a ureter in a living mouse after renal pelvic injection of Er-PLNPs (left). Scale bar, 100 μm. **g**, FWHM of the ureter shown in **f** (dashed lines) as a function of time. **h**, H&E staining results of the ureter shown in **f**. Scale bar, 100 μm. **i**, Dual-channel in vivo PL imaging of organs in a living mouse. Nd-PLNPs were used to image the gastrointestinal tract through oral administration, and Er-PLNPs were used to image visceral organs (lung, liver and spleen) via a tail vein injection. Scale bar, 1 cm. **j**, Calibrated PL intensities of visceral organs after a tail vein injection of Er-PLNPs (derived from the intensities of all the pixels in the corresponding region of interest for the lung, liver and spleen) for the Er and Ho channels. Imaging exposure time, 10 s. The data are shown as the mean ± s.d.

without excitation light (Fig. 4d). This T/N ratio is ~3.7-fold higher than that of NIR-II FL (~11.1) and outperformed most other values obtained previously with NIR-II FL, based on passive targeting (Supplementary Table 5). Although the T/N values decreased with the attenuation of NIR-II PL signals, they could still be kept above ~17.5 for 20 minutes, which is 3.5 times higher than the Rose criterion (Fig. 4d). After removing the tumour under the guidance of NIR-II PL imaging, the haematoxylin and eosin (H&E)

staining results confirmed the precise delineation of the tumour margin by the sharp cutting edge (Fig. 4e). In addition, imaging of CT-26 tumours using hydrophilic Nd-PLNPs also verified the higher contrast for NIR-II PL imaging than that for NIR-II FL imaging (Extended Data Fig. 9).

Iatrogenic ureteral injury is a feared complication of lower abdominal surgery. The special anatomical location surrounded by ~2–4 mm fat tissue and the thin-walled structure of ureters make

them difficult to identify and easy to injure[46,47]. Thus, intraoperative identification of the ureter is important to prevent iatrogenic ureteral injury and avoid postoperative complications[48]. We reasoned that NIR-II PL might enable in situ, high-contrast imaging of ureters. At 10 s p.i. of hydrophilic Er-PLNPs via the renal pelvis, the ureter was immediately illuminated by NIR-II PL signals and these nanoparticles were subsequently excreted to the bladder via the peristaltic flow of the ureters (Fig. 4f and Supplementary Fig. 25). Owing to the reduced background noise without excitation light, the SNR of the ureter was 268.5 for NIR-II PL images, which was 4.1-fold higher than that for NIR-II FL images (Supplementary Fig. 25). In addition, NIR-II PL images also revealed ureters with a sharper FWHM (180.8 versus 267 μm from the NIR-II FL images) (Fig. 4g), which is close to its real diameter (163.8 μm) measured using H&E staining (Fig. 4h). Therefore, Ln-PLNPs permitted a higher contrast imaging compared with that of NIR-II FL imaging.

The robustness of Ln-PLNPs was also supported by multiplexed in vivo imaging. We performed multiplexed NIR-II PL imaging using Nd- and Er-PLNPs to probe and differentiate multiple organs in deep tissue (Fig. 4i and Supplementary Fig. 26). Er-PLNPs were first injected into a living mouse via the tail vein, followed by gavaging of Nd-PLNPs after ten minutes. At 10 s p.i., bright NIR-II PL was seen immediately in the lungs, which correspond to the pulmonary flow of Er-PLNP-rich blood. Following the pulmonary circulation, major organs in the systemic circulation, which included the liver and spleen, also appeared (Fig. 4i,j and Supplementary Fig. 27). Although the signals in these organs decreased because of PL decay and the dynamic biodistribution of nanoparticles, these organs could still be observed with a high SNR (>65) for five minutes (Supplementary Fig. 26). In the Nd channel, intestinal peristalsis of the mouse was highlighted by the PL signal 30 minutes after gavaging and could still be resolved for 148 minutes due to the long-lasting luminescence of Nd-PLNPs (Fig. 4i and Supplementary Fig. 26). The overlayed NIR-II PL image clearly shows the main organs with a high contrast, which indicates the potential of Ln-PLNPs in deep-tissue anatomical imaging.

As they benefit from well-controlled nanostructures, Ln-PLNPs can also be engineered to develop multimodal probes. In addition to PL signals provided by the NaYF$_4$:3%Er core, we also introduced a NaGdF$_4$ shell to simultaneously enhance the PL intensity and offer T$_1$-enhanced value in magnetic resonance imaging (MRI). Moreover, ^{18}F$^-$ was further doped into the NaGdF$_4$ shell for PET imaging. Therefore, NaYF$_4$:3%Er@NaGdF$_4$-(^{18}F) PLNPs were tested in tumour-bearing mice as a trimodal imaging probe (Extended Data Fig. 10). All these data yield complementary information about the tumour, which is unavailable in previously reported PL materials.

Conclusions

Although FL spectra in the NIR-II window for in vivo bioimaging and biosensing have been investigated for over a decade[49], the investigation of PL in the same window is rare. In this work, we report a series of X-ray-activated Ln-PLNPs with a tunable NIR-II PL, controllable nanostructure and flexible construction for multifunctionality, which are not available in other existing PL materials (Supplementary Table 1). By rational core–shell design, tunable NIR-II PL signals can be imparted to single nanoparticles, which greatly enhances their encoding capacity and also adds dynamic information to improve the security of multilevel encryption. In addition, these Ln-PLNPs exhibit a low cytotoxicity[50] and good stability in aqueous solution and biological media. By eliminating excitation light-caused autofluorescence, NIR-II Ln-PLNPs show promise for high-contrast and high-resolution bioimaging in deep tissue, compared with that of conventional NIR-II FL imaging.

Although Ln-PLNPs successfully address the issue of background autofluorescence caused by interaction between the excitation light

and tissues, and also extend PL wavelengths into the NIR-II window for high-contrast in vivo imaging, the PL efficiencies of Ln-PLNPs still need to be improved for more advanced bioapplications. With brighter Ln-PLNPs, a lower X-ray dosage (below the safety threshold) with a much deeper penetration depth may be directly applied to recharge the probes in living tissues so as to realize long-term nanoprobe tracking and monitoring. Notably, the PL imaging demonstrated here is based on passive targeting. Functional molecules may be attached to highly emissive nanoparticles, not only for active targeting with a higher accumulation efficiency in more complex imaging situations, but also as intelligent activatable probes to monitor pathological processes.

Online content

Any methods, additional references, Nature Research reporting summaries, source data, extended data, supplementary information, acknowledgements, peer review information; details of author contributions and competing interests; and statements of data and code availability are available at https://doi.org/10.1038/s41565-021-00922-3.

References

1. Hong, G., Antaris, A. L. & Dai, H. Near-infrared fluorophores for biomedical imaging. *Nat. Biomed. Eng.* **1**, 0010 (2017).
2. Hu, Z. et al. First-in-human liver-tumour surgery guided by multispectral fluorescence imaging in the visible and near-infrared-I/II windows. *Nat. Biomed. Eng.* **4**, 259–271 (2019).
3. Fan, Y. et al. Lifetime-engineered NIR-II nanoparticles unlock multiplexed in vivo imaging. *Nat. Nanotechnol.* **13**, 941–946 (2018).
4. Tian, R. et al. Albumin-chaperoned cyanine dye yields superbright NIR-II fluorophore with enhanced pharmacokinetics. *Sci. Adv.* **5**, eaaw0672 (2019).
5. Carr, J. A. et al. Shortwave infrared fluorescence imaging with the clinically approved near-infrared dye indocyanine green. *Proc. Natl Acad. Sci. USA* **115**, 4465–4470 (2018).
6. Frangioni, J. V. In vivo near-infrared fluorescence imaging. *Curr. Opin. Chem. Biol.* **7**, 626–634 (2003).
7. Lu, L. et al. NIR-II bioluminescence for in vivo high contrast imaging and in situ ATP-mediated metastases tracing. *Nat. Commun.* **11**, 4192 (2020).
8. Jaunich, M., Raje, S., Kim, K., Mitra, K. & Guo, Z. Bio-heat transfer analysis during short pulse laser irradiation of tissues. *Int. J. Heat. Mass. Trans.* **51**, 5511–5521 (2008).
9. Zhan, Q. et al. Using 915 nm laser excited Tm^{3+}/Er^{3+}/Ho^{3+}-doped NaYbF$_4$ upconversion nanoparticles for in vitro and deeper in vivo bioimaging without overheating irradiation. *ACS Nano* **5**, 3744–3757 (2011).
10. Brown, C. M., Reilly, A. & Cole, R. W. A quantitative measure of field illumination. *J. Biomol. Tech.* **26**, 37–44 (2015).
11. Li, Y., Gecevicius, M. & Qiu, J. Long persistent phosphors—from fundamentals to applications. *Chem. Soc. Rev.* **45**, 2090–2136 (2016).
12. Hölsä, J. Persistent luminescence beats the afterglow: 400 years of persistent luminescence. *Electrochem. Soc. Interface* **18**, 42–45 (2009).
13. Matsuzawa, T., Aoki, Y., Takeuchi, N. & Murayama, Y. A new long phosphorescent phosphor with high brightness, SrAl$_2$O$_4$:Eu^{2+}, Dy^{3+}. *J. Electrochem. Soc.* **143**, 2670–2673 (1996).
14. le Masne de Chermont, Q. et al. Nanoprobes with near-infrared persistent luminescence for in vivo imaging. *Proc. Natl Acad. Sci. USA* **104**, 9266–9271 (2007).
15. Miao, Q. et al. Molecular afterglow imaging with bright, biodegradable polymer nanoparticles. *Nat. Biotechnol.* **35**, 1102–1110 (2017).
16. Li, Z. et al. Direct aqueous-phase synthesis of sub-10 nm 'luminous pearls' with enhanced in vivo renewable near-infrared persistent luminescence. *J. Am. Chem. Soc.* **137**, 5304–5307 (2015).
17. Maldiney, T. et al. Controlling electron trap depth to enhance optical properties of persistent luminescence nanoparticles for in vivo imaging. *J. Am. Chem. Soc.* **133**, 11810–11815 (2011).
18. Rajendran, V. et al. Super broadband near-infrared phosphors with high radiant flux as future light sources for spectroscopy applications. *ACS Energy Lett.* **3**, 2679–2684 (2018).
19. Maldiney, T. et al. The in vivo activation of persistent nanophosphors for optical imaging of vascularization, tumours and grafted cells. *Nat. Mater.* **13**, 418–426 (2014).
20. Ma, C. et al. The second near-infrared window persistent luminescence for anti-counterfeiting application. *Cryst. Growth Des.* **20**, 1859–1867 (2020).

21. Pan, Z., Lu, Y.-Y. & Liu, F. Sunlight-activated long-persistent luminescence in the near-infrared from Cr^{3+}-doped zinc gallogermanates. *Nat. Mater.* **11**, 58–63 (2012).
22. Wu, S. et al. Recent advances of persistent luminescence nanoparticles in bioapplications. *Nano-Micro Lett.* **12**, 2–26 (2020).
23. Liu, J. et al. Imaging and therapeutic applications of persistent luminescence nanomaterials. *Adv. Drug. Deliv. Rev.* **138**, 193–210 (2019).
24. Zhang, H. et al. Tm^{3+}-sensitized NIR-II fluorescent nanocrystals for in vivo information storage and decoding. *Angew. Chem. Int. Ed.* **58**, 10153–10157 (2019).
25. Xu, J. et al. 1.2 μm persistent luminescence of Ho^{3+} in $LaAlO_3$ and $LaGaO_3$ perovskites. *J. Mater. Chem. C* **6**, 11374–11383 (2018).
26. Wang, X., Chen, Y., Liu, F. & Pan, Z. Solar-blind ultraviolet-C persistent luminescence phosphors. *Nat. Commun.* **11**, 2040 (2020).
27. Abdukayum, A., Chen, J. T., Zhao, Q. & Yan, X. P. Functional near infrared-emitting Cr^{3+}/Pr^{3+} co-doped zinc gallogermanate persistent luminescent nanoparticles with superlong afterglow for in vivo targeted bioimaging. *J. Am. Chem. Soc.* **135**, 14125–14133 (2013).
28. Chen, X., Song, J., Chen, X. & Yang, H. X-ray-activated nanosystems for theranostic applications. *Chem. Soc. Rev.* **48**, 3073–3101 (2019).
29. Yang, Y.-M. et al. X-ray-activated long persistent phosphors featuring strong UVC afterglow emissions. *Light. Sci. Appl.* **7**, 88 (2018).
30. Cooper, D. R., Capobianco, J. A. & Seuntjens, J. Radioluminescence studies of colloidal oleate-capped β-Na(Gd,Lu)F_4:Ln^{3+} nanoparticles (Ln = Ce, Eu, Tb). *Nanoscale* **10**, 7821–7832 (2018).
31. Mandl, G. A. et al. On a local (de-)trapping model for highly doped Pr^{3+} radioluminescent and persistent luminescent nanoparticles. *Nanoscale* **12**, 20759–20766 (2020).
32. Ou, X. et al. High-resolution X-ray luminescence extension imaging. *Nature* **590**, 410–415 (2021).
33. Chen, G., Qiu, H., Prasad, P. N. & Chen, X. Upconversion nanoparticles: design, nanochemistry, and applications in theranostics. *Chem. Rev.* **114**, 5161–5214 (2014).
34. Wang, F. & Liu, X. Recent advances in the chemistry of lanthanide-doped upconversion nanocrystals. *Chem. Soc. Rev.* **38**, 976–989 (2009).
35. Hasse, M. & Schäfer, H. Upconverting nanoparticles. *Angew. Chem. Int. Ed.* **50**, 5808–5829 (2011).
36. Lu, Y. et al. Tunable lifetime multiplexing using luminescent nanocrystals. *Nat. Photon.* **8**, 32–36 (2014).
37. Urbach, F. Zur Lumineszenz der Alkalihalogenide: II. *Messungmethoden* **139**, 363–372 (1930).
38. Rezende, M. Vd. S., Montes, P. J. R., Andrade, A. B., Macedo, Z. S. & Valerio, M. E. G. Mechanism of X-ray excited optical luminescence (XEOL) in europium doped $BaAl_2O_4$ phosphor. *Phys. Chem. Chem. Phys.* **18**, 17646–17654 (2016).
39. Shi, H. F. & An, Z. F. Ultraviolet afterglow. *Nat. Photon.* **13**, 74–75 (2019).
40. Chen, Q. et al. All-inorganic perovskite nanocrystal scintillators. *Nature* **561**, 88–93 (2018).
41. Chernikov, A. et al. Exciton binding energy and nonhydrogenic Rydberg series in monolayer WS_2. *Phys. Rev. Lett.* **113**, 076802 (2014).
42. Jiang, Z., Liu, Z., Li, Y. & Duan, W. Scaling universality between band gap and exciton binding energy of two-dimensional semiconductors. *Phys. Rev. Lett.* **118**, 266401 (2017).
43. McClure, D. S. & Pedrini, C. Excitons trapped at impurity centers in highly ionic crystals. *Phys. Rev. B* **32**, 8465–8468 (1985).
44. Schipper, W. J. & Blasse, G. On the recombination mechanism in X-ray storage phosphors based on lanthanum fluoride. *J. Lumin.* **59**, 377–383 (1994).
45. Huang, B., Dong, H., Wong, K.-L., Sun, L.-D. & Yan, C.-H. Fundamental view of electronic structures of β-NaYF$_4$, β-NaGdF$_4$, and β-NaLuF$_4$. *J. Phys. Chem. C* **120**, 18858–18870 (2016).
46. Andersen, P., Andersen, L. M. & Iversen, L. H. Iatrogenic ureteral injury in colorectal cancer surgery: a nationwide study comparing laparoscopic and open approaches. *Surg. Endosc.* **29**, 1406–1412 (2015).
47. Minas, V., Gul, N., Aust, T., Doyle, M. & Rowlands, D. Urinary tract injuries in laparoscopic gynaecological surgery; prevention, recognition and management. *Obstet. Gynaecol.* **16**, 19–28 (2014).
48. de Valk, K. S. et al. A zwitterionic near-infrared fluorophore for real-time ureter identification during laparoscopic abdominopelvic surgery. *Nat. Commun.* **10**, 3118 (2019).
49. Smith, A. M., Mancini, M. C. & Nie, S. Second window for in vivo imaging. *Nat. Nanotechnol.* **4**, 710–711 (2009).
50. Gnach, A., Lipinski, T., Bednarkiewicz, A., Rybka, J. & Capobianco, J. A. Upconverting nanoparticles: assessing the toxicity. *Chem. Soc. Rev.* **44**, 1561–1584 (2015).

Methods

Chemical reagents. Anhydrous gadolinium(III) chloride (GdCl$_3$, 99.99%), anhydrous yttrium(III) chloride (YCl$_3$, 99.9%), anhydrous erbium(III) chloride (ErCl$_3$, 99.9%), anhydrous neodymium(III) chloride (NdCl$_3$, 99.9%), anhydrous holmium(III) chloride (HoCl$_3$, 99.9%), anhydrous thulium(III) chloride (TmCl$_3$, 99.9%), anhydrous ytterbium(III) chloride (YbCl$_3$, 99.9%), anhydrous praseodymium(III) chloride (PrCl$_3$, 99.9%), anhydrous dysprosium chloride (DyCl$_3$, 99.9%), anhydrous terbium(III) chloride (TbCl$_3$, 99.9%), anhydrous samarium(III) chloride (SmCl$_3$, 99.9%), sodium trifluoroacetate (Na-TFA, 98%), oleic acid (OA, 90%), oleylamine (OM, 70%), 1-octadecene (ODE, 90%) and nitrosyl tetrafluoroborate (NOBF$_4$, 95%) were purchased from Sigma-Aldrich. Sodium hydroxide (NaOH, 96%) and ammonium fluoride (NH$_4$F, 96%) were purchased from Sinopharm Beijing Chemical Reagents Co. Ltd. DMEM and penicillin–streptomycin was purchased from Gibco. Fetal bovine serum was purchased from Adamas-beta. All the chemicals were used as received without further purification. Yttrium(III) trifluoroacetate (Y-TFA) and erbium(III) trifluoroacetate (Er-TFA) were synthesized in our laboratory.

Preparation of shell precursors. Ln-OA (Ln = Y or Gd, 0.1 M) host precursor. A mixture of LnCl$_3$ (5.0 mM), OA (20.0 ml) and ODE (30.0 ml) was loaded into a flask and heated at 140 °C under vacuum for 60 min. A clear Ln-OA precursor solution (0.1 M) was obtained on the removal of residual water and oxygen.

Na-TFA-OA (0.4 M) host precursor. A mixture of Na-TFA (20.0 mM) and OA (50.0 ml) was loaded into a flask and heated at 70 °C under vacuum for 60 min. A clear Na-TFA-OA precursor solution (0.4 M) was obtained on removal of residual water and oxygen.

General procedure for the synthesis of Ln-PLNPs. *Synthesis of the hexagonal core Ln-PLNPs.* In a typical procedure for the synthesis of NaYF$_4$:xLn (Ln = Er, Tm, Ho, Nd, Yb, Pr, Dy, Tb or Sm) nanoparticles, $2(1-x)$ mM of YCl$_3$ and $2x$ mM LnCl$_3$ were added to a 100 ml flask that contained 50.0 ml of OA/ODE (volume ratio of 3:7). The mixture was heated to 140 °C under vacuum until a clear solution formed, after which the solution was cooled to 50 °C. Afterwards, a 10 ml methanol solution that contained NH$_4$F (8.0 mM) and NaOH (5.0 mM) was added, and the resultant solution was stirred for 30 min. After the methanol was removed, the solution was heated to 290 °C at a rate of 10 °C min^{-1}, maintained for 1.5 h under an argon atmosphere and then cooled to room temperature. Hexagonal core nanoparticles were obtained by centrifugation, washed with ethanol three times and redispersed in 10 ml of cyclohexane. In addition, the size of the core nanoparticles can be easily tuned by reducing the volume of OA/ODE, without changing the core composition. For example, the size of the NaYF$_4$:3%Er nanoparticles increased from about 22.7 to 35.0 to 63.2 to 84.3 nm when the volume of OA/ODE was reduced from 50.0 to 25 to 22 to 18.0 ml, respectively.

Synthesis of hexagonal core–shell Ln-PLNPs. In a typical procedure for the synthesis of NaYF$_4$:xLn$_1$@NaLn$_2$F$_4$ (Ln$_1$ = Er, Nd, Ho or Tm; Ln$_2$ = Y or Gd) nanoparticles, 1.0 ml of colloidal NaYF$_4$:xLn core nanoparticles (~0.2 mM) was mixed with 3.2 ml of OA and 4.8 ml of ODE in a flask. The flask was kept at 70 °C under vacuum for 30 min. On removal of cyclohexane and residual air, the solution was heated to 280 °C at a rate of 10 °C min^{-1} under an argon atmosphere. Then, a mixture of Y–OA or Gd–OA (0.1 M, 6.0 ml) and Na-TFA–OA (0.40 M, 3.0 ml) was added dropwise (3.0 ml h^{-1}) at 280 °C. Finally, the obtained hexagonal core–shell NaYF$_4$:xLn$_1$@NaLn$_2$F$_4$ nanoparticles were precipitated and washed in the same way as for the core nanoparticles, followed by redispersion in 1.0 ml of cyclohexane. In addition, the shell thickness was tuned by changing the precursor volume. Take NaYF$_4$:3%Er@NaYF$_4$ nanoparticles as an example, the shell thickness of the NaYF$_4$:3%Er core nanoparticles (22.7 nm) increased from 0, 2.8, 4.7 to 6.5 nm when the volume of the shell precursors (a mixture of Y-OA and Na-TFA–OA) was increased from 0, 3, 6 to 9 ml, respectively.

Multilayered Er/Nd/Ho-PLNPs (NaYF$_4$:1%Ho@NaGdF$_4$@ NaYF$_4$:3%Er@NaGdF$_4$@NaYF$_4$:1%Nd@NaGdF$_4$) and co-doped Er/Nd/Ho-PLNPs (NaYF$_4$:1%Ho, 3%Er,1%Nd@NaGdF$_4$) were obtained using the method described above.

Synthesis of cubic core–shell Er-PLNPs. In a typical procedure for the synthesis of cubic Er-PLNPs (NaYF$_4$:3%Er@ NaYF$_4$), 1 mM Na-TFA, 0.97 mM Y-TFA and 0.03 mM Er-TFA were added to a 100 ml three-necked flask that contained 10 mM OA, 10 mM OM and 20 mM ODE. The flask was heated at 100 °C under vacuum for 30 min to remove water and residual air. Subsequently, the solution was heated to 310 °C for 15 min at a rate of 15 °C min^{-1} under argon. After cooling to room temperature, cubic NaYF$_4$:3%Er (~6 nm) nanoparticles were obtained by centrifugation, washed with ethanol three times and redispersed in 5.0 ml of cyclohexane. The obtained core nanoparticles (6 nm) were used as seeds and added into a 50 ml three-necked flask that contained 20 mM Na-TFA, 19.4 mM Y-TFA, 0.6 mM Er-TFA, 10 mM OA and 10 mM ODE. The flask was heated at 100 °C under vacuum for 30 min to remove water and residual air. Subsequently, the solution was heated to 290 °C for 40 min at a rate of 15 °C min^{-1} under argon. After cooling to room temperature, the size of the obtained cubic NaYF$_4$:3%Er nanoparticles had increased to 22.1 nm. To finally prepare the cubic core–shell

Er-PLNPs (NaYF$_4$:3%Er@NaYF$_4$), the above-obtained NaYF$_4$:3%Er (22.1 nm) nanoparticles were used as seeds and added into a 50 ml three-necked flask that contained 3 mM Na-TFA, 3 mM Y-TFA, 10 mM OA and 10 mM ODE. The flask was heated at 100 °C under vacuum for 30 min to remove water and residual air. Subsequently, the solution was heated to 290 °C for 40 min at a rate of 15 °C min^{-1} under argon. After cooling to room temperature, cubic NaYF$_4$:3%Er@NaYF$_4$ (31.3 nm) nanoparticles were obtained and redispersed in 5.0 ml of cyclohexane for benchmarking with hexagonal Er-PLNPs.

General procedure for the preparation of water-soluble Ln-PLNPs for biological applications. The as-prepared OA-capped Ln-PLNPs (1.0 ml, 0.2 mM) and NOBF$_4$ (100 mg) were added to dimethylformamide (3.0 ml) and ultrasonicated for 2 min to remove surface OA. The liquid was stratified with nanoparticles on the bottom dimethylformamide layer after standing for 5 min. OA-free nanoparticles were obtained by removing the top cyclohexane layer and washing with ethanol three times. Finally, 1.0 ml of H$_2$O was added to the obtained OA-free nanoparticles, to form a clear solution.

General procedure for the preparation of NaYF$_4$:3%Er@NaGdF$_4$-(^{18}F) nanoparticles for multimodal imaging. To prepare NaYF$_4$:3%Er@NaGdF$_4$-(^{18}F) nanoparticles for multimodal imaging, a NaGdF$_4$ shell (thickness of ~7 nm, 0.6 mM) was introduced onto the NaYF$_4$:3%Er core nanoparticles (~20 nm, 0.1 mM) to offer a longitudinal (T_1)-enhanced value in the MRI. The concentration of Gd^{3+} was determined by an inductively coupled plasma atomic emission spectrometer (iCAP 7400, ThermoFisher Scientific). The T_1 proton magnetic relaxation time of NaYF$_4$:3%Er@NaGdF$_4$ was analysed with a 1.41 T NMR analyser (minispec mq 60, Bruker) at 37 °C. The relaxation rate R_1 was determined by measuring $1/T_1$ slope to the corresponding Gd^{3+} concentrations. Then the as-prepared NaYF$_4$:3%Er@NaGdF$_4$ (0.2 mM in H$_2$O, 500 μl) was mixed with 0.5 ml of an aqueous solution of ^{18}F(~400 MBq) at room temperature, followed by sonication for 10 min. NaYF$_4$:3%Er@NaGdF$_4$-(^{18}F) nanoparticles were obtained by centrifugation and washing with distilled water three times under ultrasonication. Finally, 500 μl of H$_2$O were added before further use. Radio thin-layer chromatography analysis indicated a 96% yield in labelling NaYF$_4$:3%Er@NaGdF$_4$ nanoparticles with ^{18}F (~184 MBq).

General procedure for the preparation of Ln-PLNP-encapsulated PDMS beads and butterfly pattern. *PDMS beads.* In a typical experiment, Ln-PLNPs (50–200 μl, 0.2 mM in chloroform) were added into a PDMS solution (Sylgard 184, Dow Corning, with a curing agent in a 10:1 ratio, 100 μl), and the mixture was drop cast on a bead mould. PLNP-encapsulated PDMS beads were obtained after heating at 90 °C for 60 min.

PDMS butterfly pattern. In a typical experiment, multilayered Er/Ho-PLNPs (50–200 μl, 0.2 mM in chloroform) were added into a PDMS solution (100 μl), and the mixture was drop cast on the different windows of a butterfly mould. A PLNP-encapsulated PDMS butterfly pattern was obtained after heating at 90 °C for 60 min.

Animal handling. All the animal procedures were in agreement with the guidelines of the Fudan Institutional Animal Care and Use Committee and performed accordingly. BALB/c mice (6–8 weeks, female, with an average weight of 20 g) and ICR mice (8–10 weeks, male, with an average weight of 30 g) were purchased from the Shanghai SLRC Laboratory Animal Centre. The surrounding relative humidity level was 55–65% and the temperature was ~25 °C. The hair of the BALB/c mice was carefully removed using Nair to avoid causing wounds to the skin. To prepare the subcutaneous tumour model, the BALB/c mice were inoculated subcutaneously with CT-26 or 4T1 cells (10–50 μl, 1 × 10^7 cells ml^{-1}). CT-26 or 4T1 cells (5 × 10^5 per dish) were seeded in a cell culture flask in 8 ml of DMEM medium supplemented with 10% fetal bovine serum and 1% antibiotics and incubated in CO$_2$ for 24 h at 37 °C prior to preparing the tumour model. NIR-II PL and NIR-II FL in vivo imaging were conducted on a homemade NIR-II imaging system equipped with an InGaAs CCD (charge-coupled device) camera (NIRvana 640, Princeton Instruments; 640 × 512 pixels).

General materials characterization. TEM and high-resolution TEM were performed using a JEM-2100F transmission electron microscope with an accelerating voltage of 200 kV equipped with a postcolumn Gatan imaging filter (GIF-Tridiem). X-ray diffraction measurements were performed at room temperature on a Bruker D8 diffractometer using Cu Kα radiation (wavelength = 1.5406 Å). The FL spectra were measured using an Edinburgh FLS980 spectroscope. X-ray luminescence spectra and PL emission spectra were measured using Ideaoptics NIR1700 and NOVA fibre optic spectrometers. A benchtop X-ray source (JF-2000, Dandong Aolong Radiographic Instrument Group Co., Ltd.) with a 50 kV and 30 mA tungsten target was used to the activate PLNPs for X-ray luminescence and PL measurements. The NIR-II PL images of all the Ln-PLNPs were obtained on the homemade NIR-II imaging system, which included an InGaAs CCD camera (NIRvana 640, Princeton Instruments; 640 × 512 pixels). For imaging in the Er channel, a 850 longpass filter, a 1000 longpass filter

and a 1400 longpass filter were adopted. For imaging in Ho channel, a 850 longpass filter, a 1100 longpass filter and a 1300 shortpass filter were adopted. For imaging in Nd channel, an 850 longpass filter, a 1,000 longpass filter and a 1,100 shortpass filter were adopted. For imaging in the full channel, an 850 longpass filter, a 1,000 longpass filter were adopted to eliminate light interference below 1,000 nm.

The decay curves of PL. *The NIR-II PL decay.* The decay curves of NIR-II PL were obtained on the homemade NIR-II imaging system, which included an InGaAs CCD camera. For a fair comparison, all the samples were tested at the same concentration of 0.2 mM in cyclohexane or other solvents. Before testing, all the samples were irradiated with X-rays of the same dosage (~200 Gy). Then the CCD collected a series of images in the time dimension. The NIR-II PL intensities of the region of interest were extracted by the MATLAB software package at different time intervals, which are displayed as the mean intensity of all pixels within the corresponding region of interest. Finally, the NIR-II PL decay curves present as a function of PL intensity and time.

Visible PL decay. Visible PL images were obtained on a SCMOS camera (Dhyana 400BSI). The data collection was similar to that for NIR-II PL.

The TL curves of Ln-PLNPs. The TL curves of Ln-PLNPs were measured on a TOSL-3DS (RongFan Tech) TL reader at a heating rate of $1\,°C\,s^{-1}$ from room temperature to $400\,°C$. All the samples were pre-irradiated by X-ray (~200 Gy) and then were stored in a dark box for 24 h at room temperature before the TL measurements.

The cytotoxicity of Ln-PLNPs. The cytotoxicity was measured using a Cell Counting Kit-8 (CCK-8) assay in 4T1 and HEK-293 cells. The cells (1×10^4) were incubated in each well of a 96-well plate for 24 h, then incubated with Er-PLNPs or Nd-PLNPs with different concentrations for 24 h, after being washed by PBS (pH = 7.4, once) three times. The WST-8 in this kit was reduced by the dehydrogenases in living cells to give a yellow-coloured product (formazan). The quality was assessed calorimetrically by using a microplate reader (Bio Tek, SYNERGY2). The measurements were based on the absorbance values at 450 nm. The formula used to calculate the viability of cell growth was: viability (%) = (mean absorbance value of treatment group/mean absorbance value of control group) × 100.

In vivo imaging of blood vessels and ureters. *Imaging of blood vessels.* The pre-irradiated Er-PLNPs (100 μl, 0.2 mM in H_2O) were injected into BALB/c mice via an abdominal vein using a homemade syringe. The bevel of the needle was first inserted into the coeliac vein and secured using tissue adhesive. The plastic tubing was then connected to a syringe (30-gauge needle) prefilled with the Ln-PLNPs of interest. NIR-II PL images were obtained using an InGaAs CCD camera over time with a 10 s exposure time. The NIR-II FL was excited by an 808 nm laser (power, $3\,mW\,cm^{-2}$).

Imaging of ureters. ICR mice were anaesthetized with avertin (1.25%, 100 μl per 10 g), and then the abdominal skin and muscle layers were incised to expose the kidney, ureter and bladder. The pre-irradiated Er-PLNPs (50 μl, 0.2 mM in H_2O) were locally injected into the renal pelvis of living mice (ICR, 8 weeks, with an average weight of 30 g) to compare the PL imaging with the FL imaging. NIR-II PL images were obtained using an InGaAs CCD camera over time with a 10 s exposure time. The NIR-II FL was excited by an 808 nm laser (power, $3\,mW\,cm^{-2}$).

In vivo imaging of tumours. *Intratumoural injection.* The pre-irradiated Nd-PLNPs (2–15 μl, 0.2 mM in H_2O) were locally injected into a tumour site to compare the PL imaging with the FL imaging. NIR-II PL images were firstly obtained using an InGaAs CCD camera over time with a 10 s exposure time. The NIR-II FL was excited by an 808 nm laser (power, $2–4\,mW\,cm^{-2}$).

Intravenous injection. The pre-irradiated Er-PLNPs (40 μl four times, 0.2 mM in H_2O) were injected into tumour-bearing mice via an abdominal vein using a homemade syringe. The bevel of the needle was first inserted into the coeliac vein and secured using tissue adhesive. The plastic tubing was then connected to a syringe (30-gauge needle) prefilled with the Ln-PLNPs of interest. NIR-II PL images were obtained using an InGaAs CCD camera over time with a 10 s exposure time. The NIR-II FL was excited by an 808 nm laser (power, $3\,mW\,cm^{-2}$).

In vivo imaging of dual-channel PL. Er-PLNPs (0.2 mM in H_2O) and Nd-PLNPs (0.2 mM in H_2O) were pre-irradiated by X-rays and stored at $-20\,°C$ prior to imaging. Er-PLNPs (100 μl) were first injected into a BALB/c mouse via the tail vein, followed by orally administering Nd-PLNPs (300 μl) 10 min later. PL imaging was obtained using the homemade NIR-II imaging system with a 10 s exposure time.

Multimodal in vivo imaging of tumour. *PL imaging.* The pre-irradiated NaYF$_4$:3%Er@NaGdF$_4$ nanoparticles (25 μl, 0.2 mM in H_2O) were locally injected into the tumour site. The homemade NIR-II imaging system was used to record the NIR-II PL images with a 10 s exposure time.

MRI. NaYF$_4$:3%Er@NaGdF$_4$ nanoparticles (25 μl, 0.2 mM in H_2O) were locally injected into the tumour site. In vivo MRI was conducted on a 3 T MRI scanner

with a receiver coil for mice (Chenguang Med Tech), using a T1-mapping sequence (repetition time, 600 ms; echo time, 20 ms; flip angle, 90°; field of view, 50×50 mm; voxel size, $0.2 \times 0.198 \times 1.0$ mm; slice gap, 0.5 mm; slice thickness, 1.0 mm). Mice were scanned before and after the nanoparticle injection, and transversal cross-section images were obtained.

PET imaging. NaYF$_4$:3%Er@NaGdF$_4$-(^{18}F) nanoparticles (~50 μCi, 0.2 mM in H_2O) were locally injected into the tumour site. PET images were recorded using a Siemens Inveon small-animal PET scanner.

Special notes. The Ln-PLNPs used for the measurements and applications were of hexagonal phase and dispersed in cyclohexane (0.2 mM), and were all pre-irradiated with X-rays (~200 Gy), except as otherwise specified. For a fair comparison, the first captured image was chosen to calculate the PL intensity after X-ray irradiation ceased. In addition, PL images obtained in the NIR-II window are presented with pseudocolour in the logarithmic PL intensity for a better visual effect.

Statistics and reproducibility. Values are shown as the mean ± s.d. All the experiments were performed at least three times independently and the replicate samples are indicated as *n*.

Reporting Summary. Further information on research design is available in the Nature Research Reporting Summary linked to this article.

Data availability
The data that support the plots within this paper and other findings of this study are available from the corresponding author upon reasonable request. Source data are provided with this paper.

Code availability
The code that has been used for this work is available from the corresponding author upon request.

References
51. Liu, Q. et al. ^{18}F-labeled magnetic-upconversion nanophosphors via rare-earth cation-assisted ligand assembly. *ACS Nano* **5**, 3146–3157 (2011).
52. Xiudong, Shi et al. Hemoglobin-mediated biomimetic synthesis of paramagnetic O$_2$-evolving theranostic nanoprobes for MR imaging-guided enhanced photodynamic therapy of tumor. *Theranostics* **10**, 11607–11621 (2020).

Acknowledgements

Author contributions
F.Z., Y.F. and Y.Y. conceived and designed experiments. P.P. synthesized the nanoparticles and conducted the PL coding experiments. Y.C. and P.P. conducted the imaging of the blood vessels, ureters and tumours. P.P. and C.S. conducted the dual-channel imaging of the organs and multimodel tumour imaging. H.Z., Y.F. and P.P. built the NIR-II imaging system. Xuan Liu and L.L. developed the codes for image processing. P.P., F.Z. and Y.F. wrote the manuscript. F.Z., Y.F., Y.Y., P.P., Xiaogang Liu, M.Z. and H.Z. analysed the results, figures and supplementary information. F.Z., Y.F., Y.Y., P.P., Xiaogang Liu and D.Z. discussed the mechanism of PL in these Ln-based nanoparticles. D.Z. and F.Z. also contributed to the discussions about the experimental approaches to imaging of the blood vessels and ureters. All the authors contributed to discussing and editing the manuscript.

Competing interests
The authors declare no competing interests.

Additional information
Extended data is available for this paper at https://doi.org/10.1038/s41565-021-00922-3.

Supplementary information The online version contains supplementary material available at https://doi.org/10.1038/s41565-021-00922-3.

Correspondence and requests for materials should be addressed to Y.F., Y.Y. or F.Z.

Peer review information *Nature Nanotechnology* thanks Cyrille Richard and the other, anonymous, reviewer(s) for their contribution to the peer review of this work.

**Reprints and permissions information** is available at www.nature.com/reprints.
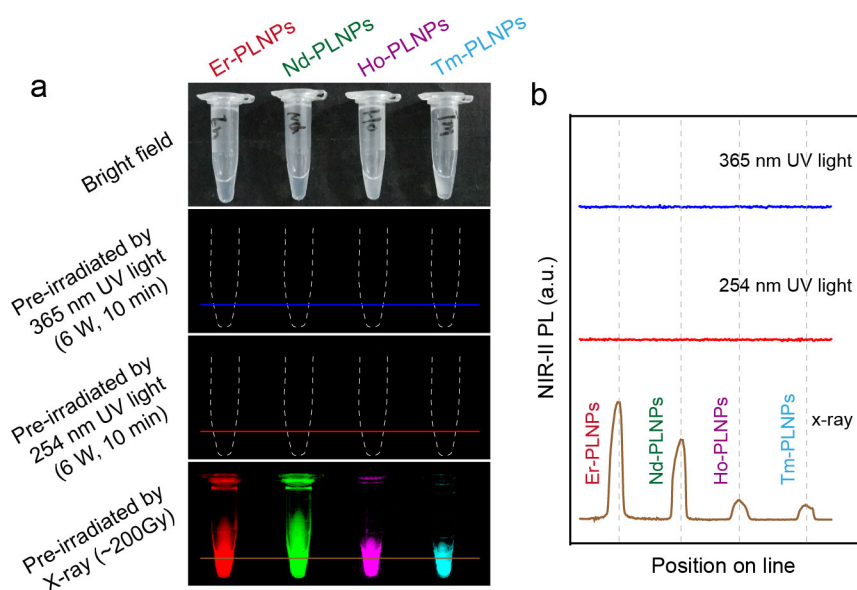
Extended Data Fig. 1 | Influence of the excitation light on the persistent luminescence of Ln-PLNPs. a, NIR-II PL images of Er-PLNPs (NaYF$_4$:3%Er@NaYF$_4$), Nd-PLNPs (NaYF$_4$:1%Nd@NaYF$_4$), Ho-PLNPs (NaYF$_4$:1%Ho@NaYF$_4$) and Tm-PLNPs (NaYF$_4$:1%Tm@NaYF$_4$) after being pre-irradiated with UV light (254 nm and 365 nm, 6 W for 10 min irradiation) or X-rays (~200 Gy). **b**, the corresponding intensity profiles of NIR-II PL images in **a**. Due to the large bandgap of fluoride hosts of Ln-PLNPs, high-energy X-rays are necessary to generate persistent luminescence in the NIR-II window.
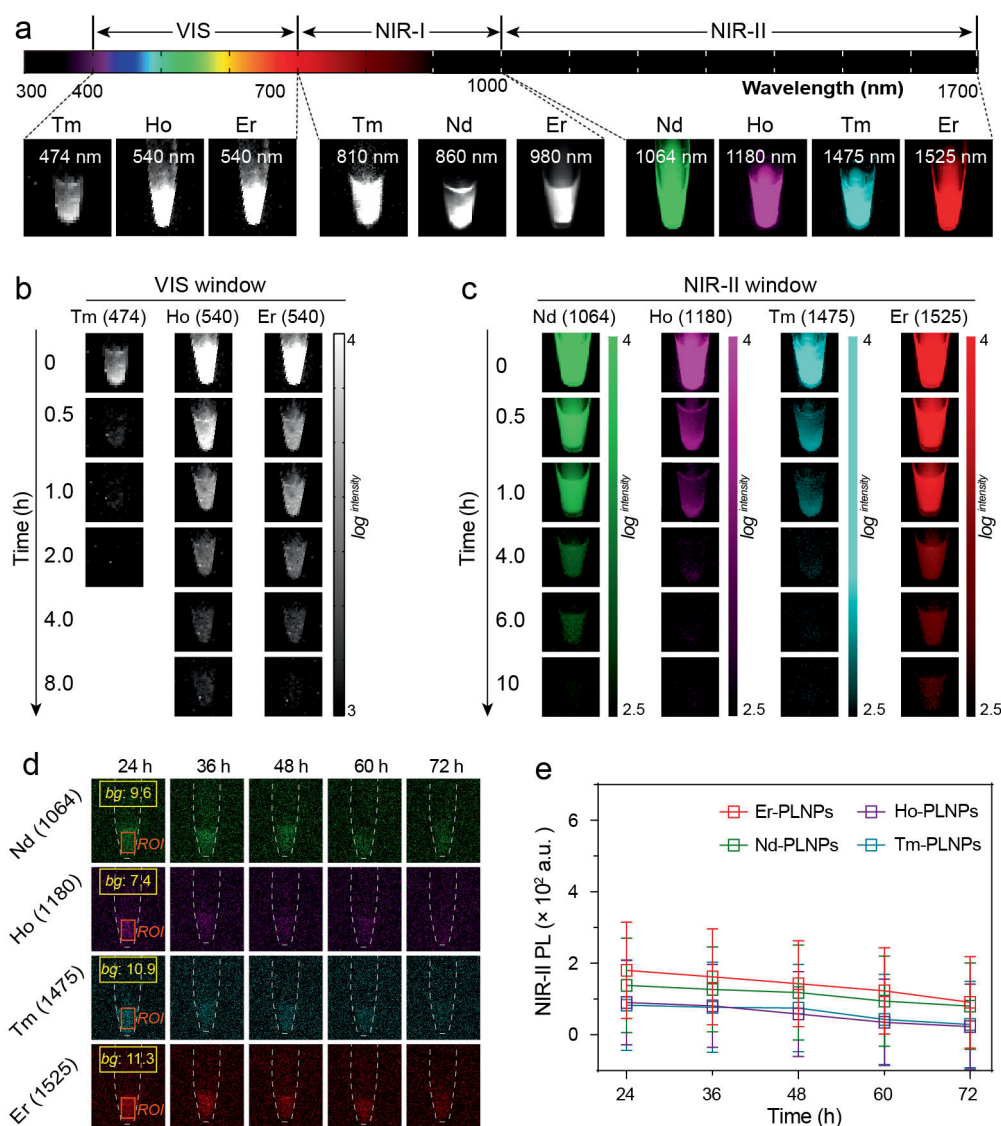
Extended Data Fig. 2 | Persistent luminescence images of various Ln-PLNPs in the visible-NIR region. a, PL images of centrifuge tubes, filled with hexagonal Er-PLNPs (NaYF$_4$:3%Er@NaYF$_4$), Nd-PLNPs (NaYF$_4$:1%Nd@NaYF$_4$), Ho-PLNPs (NaYF$_4$:1%Ho@NaYF$_4$), and Tm-PLNPs (NaYF$_4$:1%Tm@NaYF$_4$), recorded at different emission bands. **b, c, d**, Corresponding long-lasting properties of Er-PLNPs, Nd-PLNPs, Ho-PLNPs, and Tm-PLNPs in the VIS emission bands (**b**), and NIR-II emission bands (**c, d**) shown in **a**. *bg:* background, *ROI*: region of interest. **e**, Corresponding NIR-II PL signal intensities of Er-PLNPs, Nd-PLNPs, Ho-PLNPs, and Tm-PLNPs shown in **d** (*n* = the number of pixels within the corresponding *ROI*). Imaging exposure time for VIS and NIR-II images are 1 s and 5 s, respectively. The data are shown as the mean ± s.d.
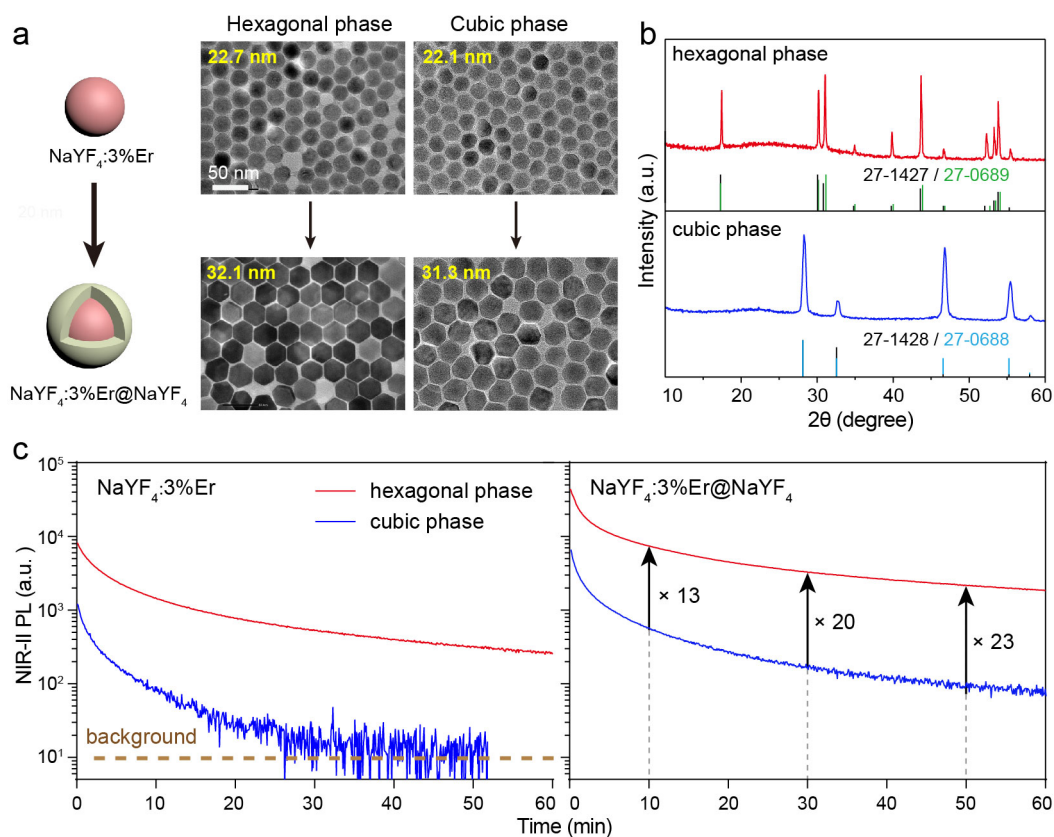
Extended Data Fig. 3 | Comparison of the influence of crystal phase on NIR-II persistent luminescence. a, TEM images of cubic and hexagonal Er-PLNPs with core ($NaYF_4$:3%Er) and core-shell ($NaYF_4$:3%Er@$NaYF_4$) structures. **b**, XRD pattern of cubic and hexagonal core-shell Er-PLNPs. The standard diffraction patterns of hexagonal $NaErF_4$ (JCPDS 27–0689), hexagonal $NaYF_4$ (JCPDS 27–1427), cubic $NaErF_4$ (JCPDS 27–0688) and cubic $NaYF_4$ (JCPDS 27–1428) are included for references. **c**, Corresponding NIR-II PL decay curves of cubic and hexagonal Er-PLNPs with bare core and core-shell structure. NIR-II PL signals of hexagonal $NaYF_4$:3%Er@$NaYF_4$ were about 13, 20, and 23 times higher than that of cubic $NaYF_4$:3%Er@$NaYF_4$ at 10 min, 30 min, and 50 min, respectively, probably due to a reduced level of crystal defects or internal quenching. Decay curves were abstracted from corresponding NIR-II PL images with 5 s exposure time.
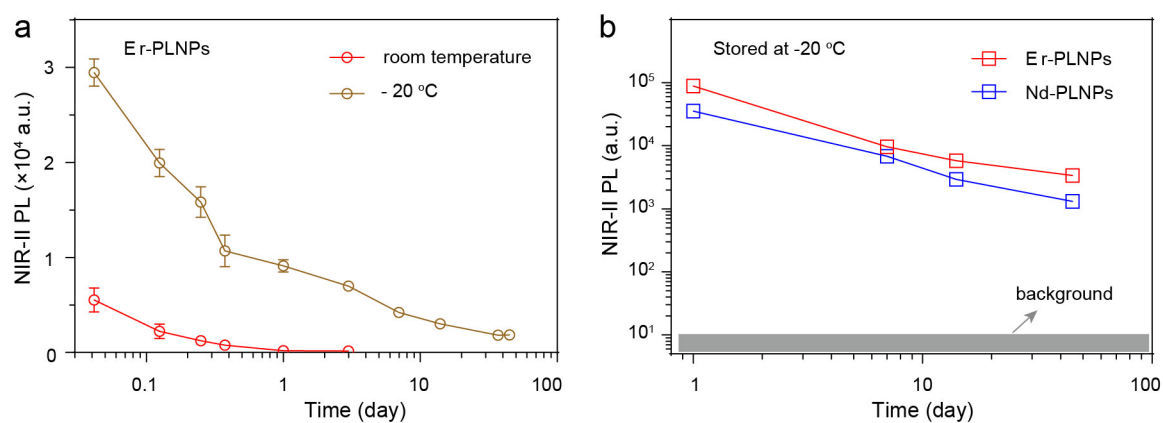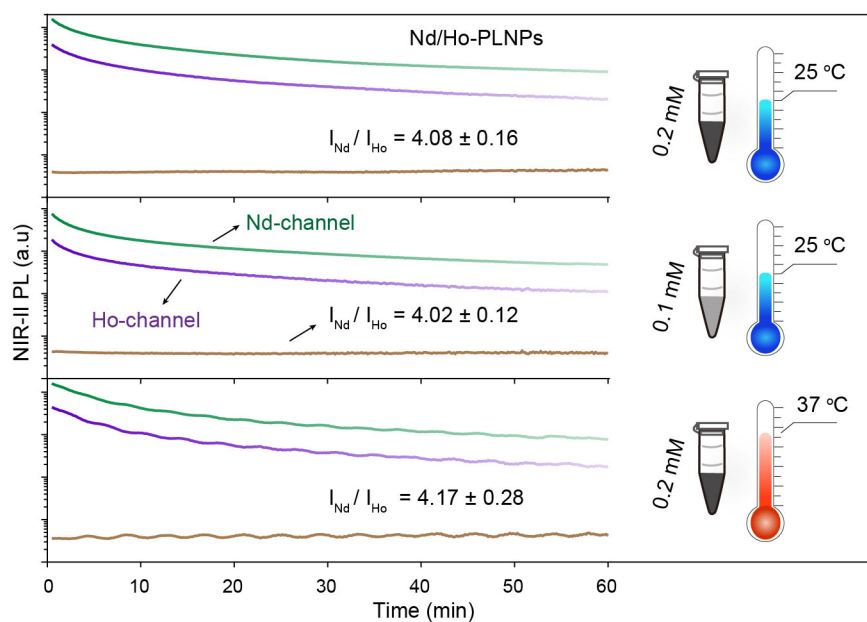
Extended Data Fig. 4 | Influence of storage temperature on the NIR-II persistent luminescence of Er-PLNPs (NaYF$_4$:3%Er@NaYF$_4$) and Nd-PLNPs (NaYF$_4$:1%Nd@NaYF$_4$). a, Storable NIR-II PL of Er-PLNPs (0.2 mM in cyclohexane) at room temperature and −20 °C as a function of time. **b**, Storable NIR-II PL of Er-PLNPs and Nd-PLNPs powders (0.2 mM) stored at −20 °C as a function of time. n = 3 independent experiments. NIR-II PL signals were abstracted from corresponding images with 5 s exposure time. The data are shown as the mean ± s.d.
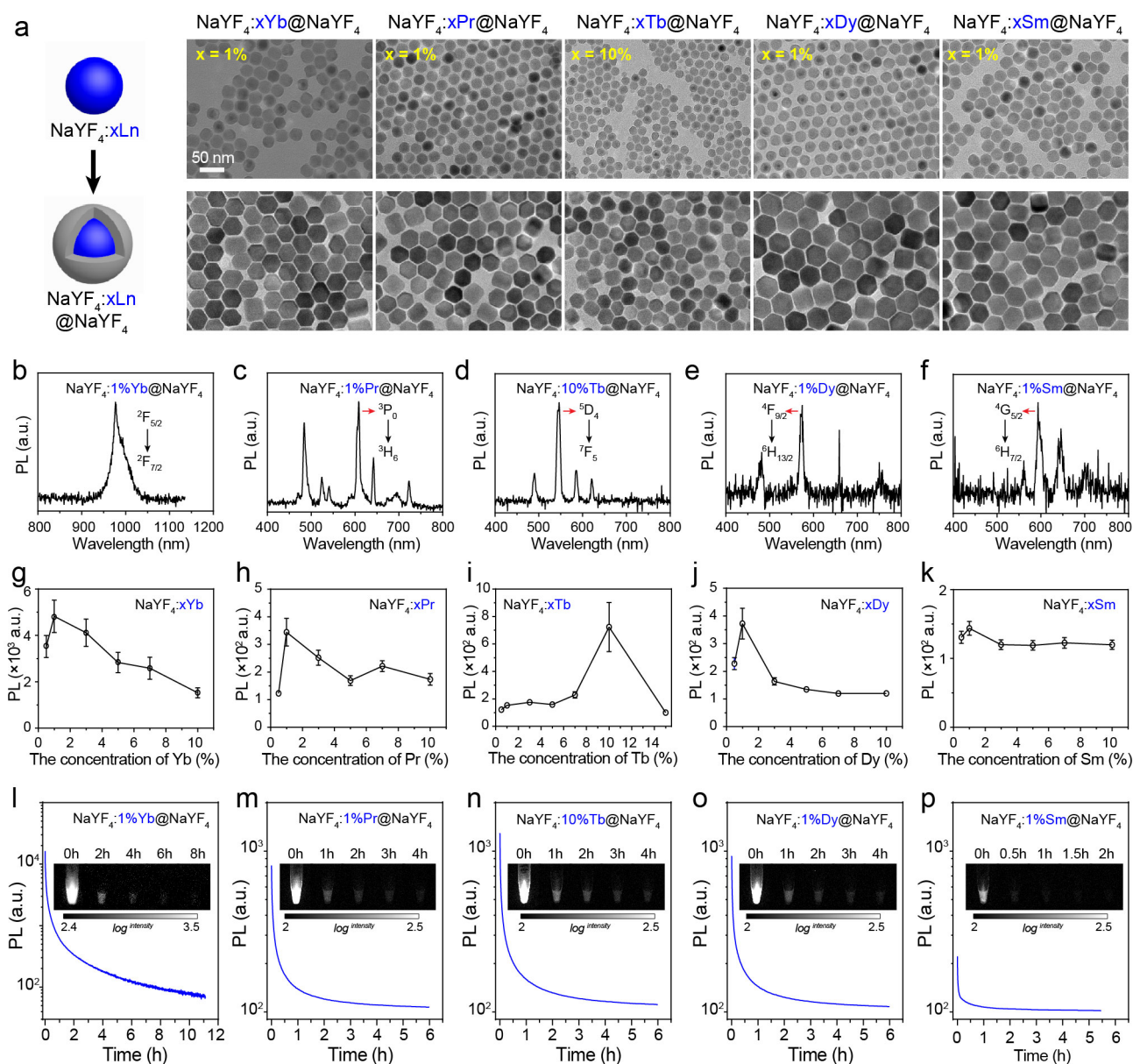
Extended Data Fig. 5 | Persistent luminescence properties of Ln-PLNPs with Yb³⁺, Pr³⁺, Tb³⁺, Dy³⁺ and Sm³⁺ as the activators. a, TEM images of Yb-PLNPs (NaYF₄:1%Yb@NaYF₄), Pr-PLNPs (NaYF₄:1%Pr@NaYF₄), Tb-PLNPs (NaYF₄:1%Tb@NaYF₄), Dy-PLNPs (NaYF₄:10%Tb@NaYF₄) and Sm-PLNPs (NaYF₄:1%Sm@NaYF₄), respectively. **b, g, l**, PL spectra (**b**), Influence of activator concentration (**g**), and PL decay curve (**l**) of Yb-PLNPs. **c, h, m**, PL spectra (**c**), Influence of activator concentration (**h**), and PL decay curve (**m**) of Pr-PLNPs. **d, i, n**, PL spectra (**d**), Influence of activator concentration (**i**), and PL decay curve (**n**) of Tb-PLNPs. **e, j, o**, PL spectra (**e**), Influence of activator concentration (**j**), and PL decay curve (**o**) of Dy-PLNPs. **f, k, p**, PL spectra (**f**), Influence of activator concentration (**k**), and PL decay curve (**p**) of Sm-PLNPs. $n = 3$ independent experiments. Yb-PLNPs were imaged using an InGaAs CCD camera with 5 s exposure time; Pr-PLNPs, Tb-PLNPs, Dy-PLNPs and Sm-PLNPs were imaged using a SCMOS camera with 1 s exposure time. The data are shown as the mean ± s.d.
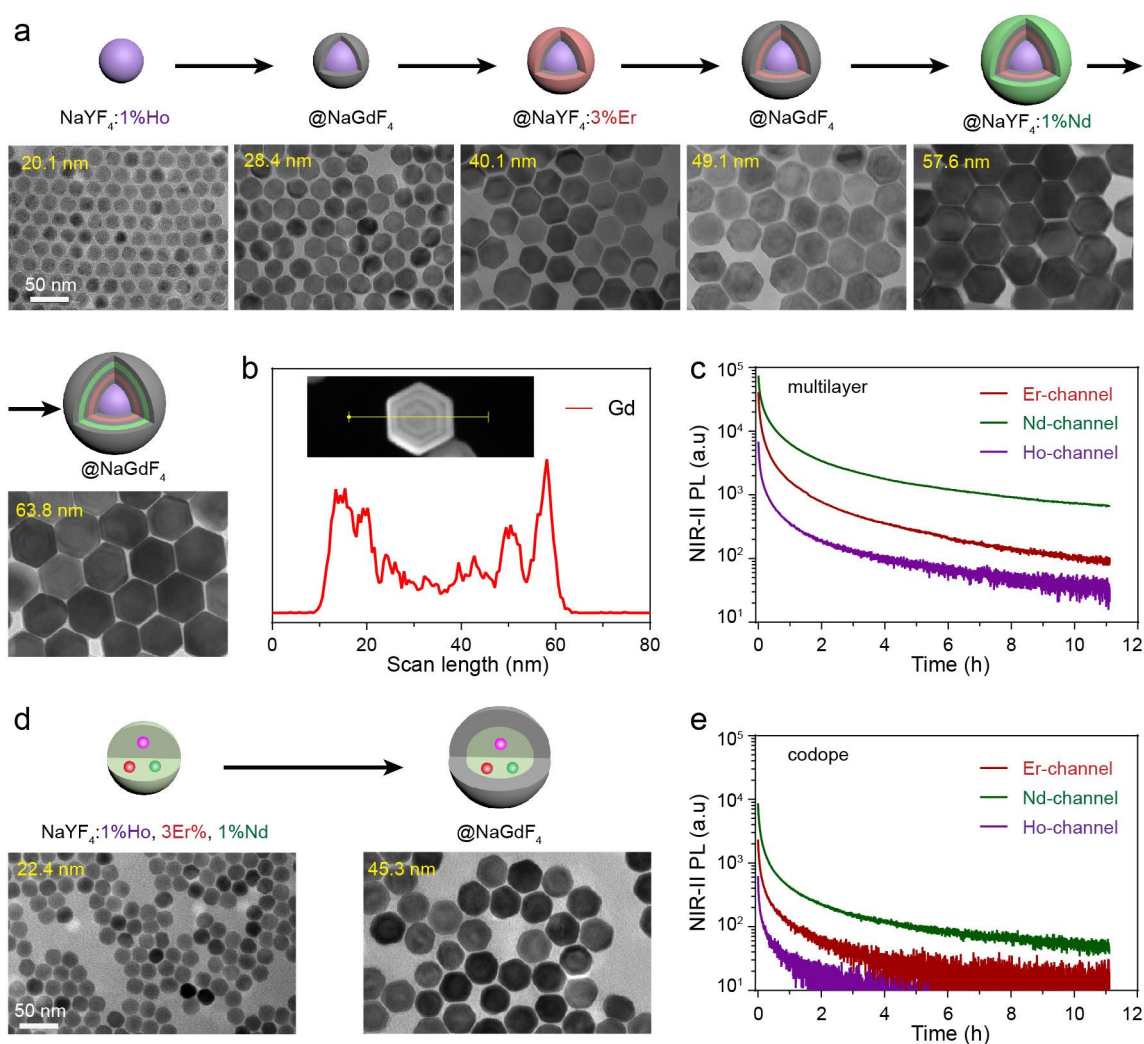
Extended Data Fig. 6 | Synthesis and characterization of multilayered and codoped Ln-PLNPs. a, Synthesis process and corresponding TEM images of multilayered Er/Nd/Ho-PLNPs. **b**, Electron energy-loss spectroscopy (EELS) line scan, conducted with HAADF-STEM imaging (inset) on a multilayered Er/Nd/Ho-PLNP, showing that Gd signals in different regions of the crystal are consistent with the designed multilayered structure. **c**, The corresponding NIR-II PL decay curves of multilayered Er/Nd/Ho-PLNPs in Er-channel, Nd-channel, and Ho-channel, respectively. **d**, Synthesis process and corresponding TEM images of codoped Er/Nd/Ho-PLNPs. **e**, The corresponding NIR-II PL decay curves of codoped Er/Nd/Ho-PLNPs in Er-channel, Nd-channel and Ho-channel, respectively. NIR-II PL decay curves were abstracted from corresponding images with 5 s exposure time.

Extended Data Fig. 7 | Influence of sample concentration and temperature on the ratio of persistent luminescence signals. Although the PL signals of Nd-channel and Ho-channel in multilayered Nd/Ho-PLNPs ($NaYF_4$:1%Ho@$NaGdF_4$@$NaYF_4$:1%Nd@$NaGdF_4$) both decay over time, the PL ratio (I_{Nd}/I_{Ho}) between the two channels is consistent, independent of sample concentration, surrounding temperature and PL signal duration. NIR-II PL decay curves were abstracted from corresponding images with 5 s exposure time.
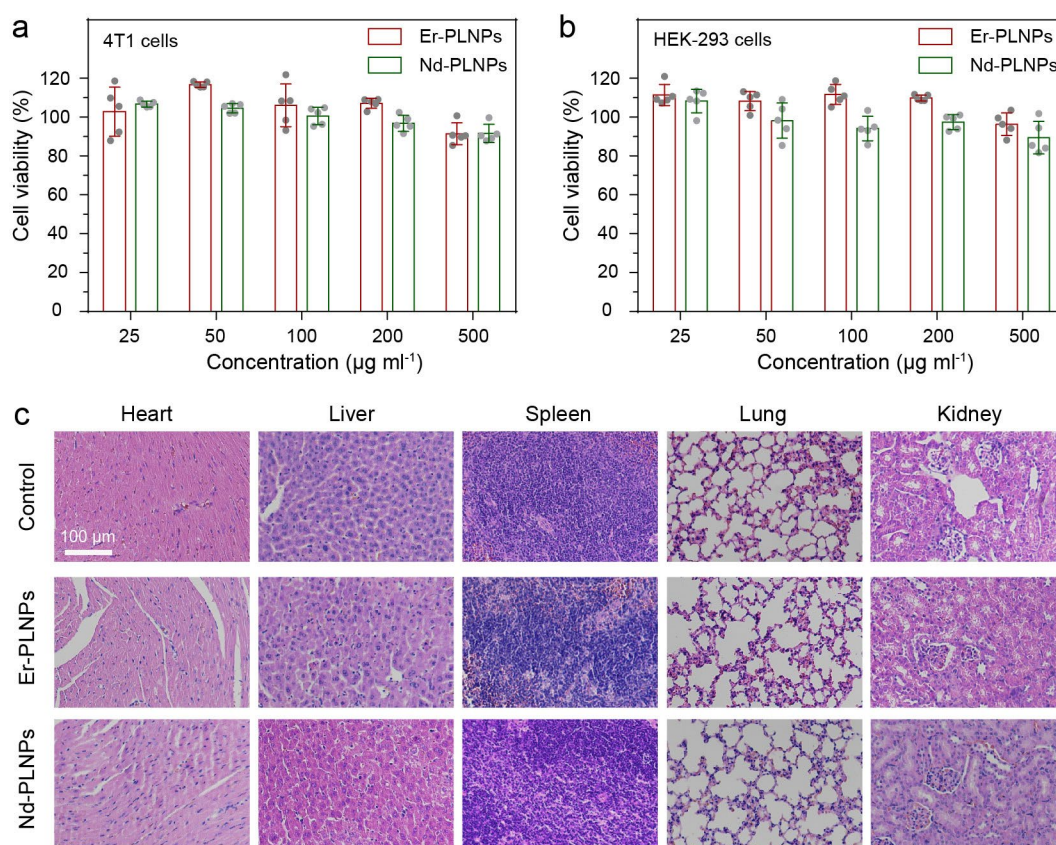
Extended Data Fig. 8 | The biocompatibility of Ln-PLNPs. a,b, cell viabilities of 4T1 cells (**a**) and HEK-293 cells (**b**) incubated with Er-PLNPs and Nd-PLNP for 24 hours. $n = 5$ independent experiments. **C**, H&E staining of visceral organs (heart, liver, spleen, lung and kidney), obtained at 24 h post-injection of H_2O (100 μL, control group), Er-PLNPs or Nd-PLNPs (0.2 mM in H_2O, 100 μL) via the tail vein. These results indicated that Er-PLNPs and Nd-PLNPs have good biocompatibility and low toxicity. The data are shown as the mean ± s.d.
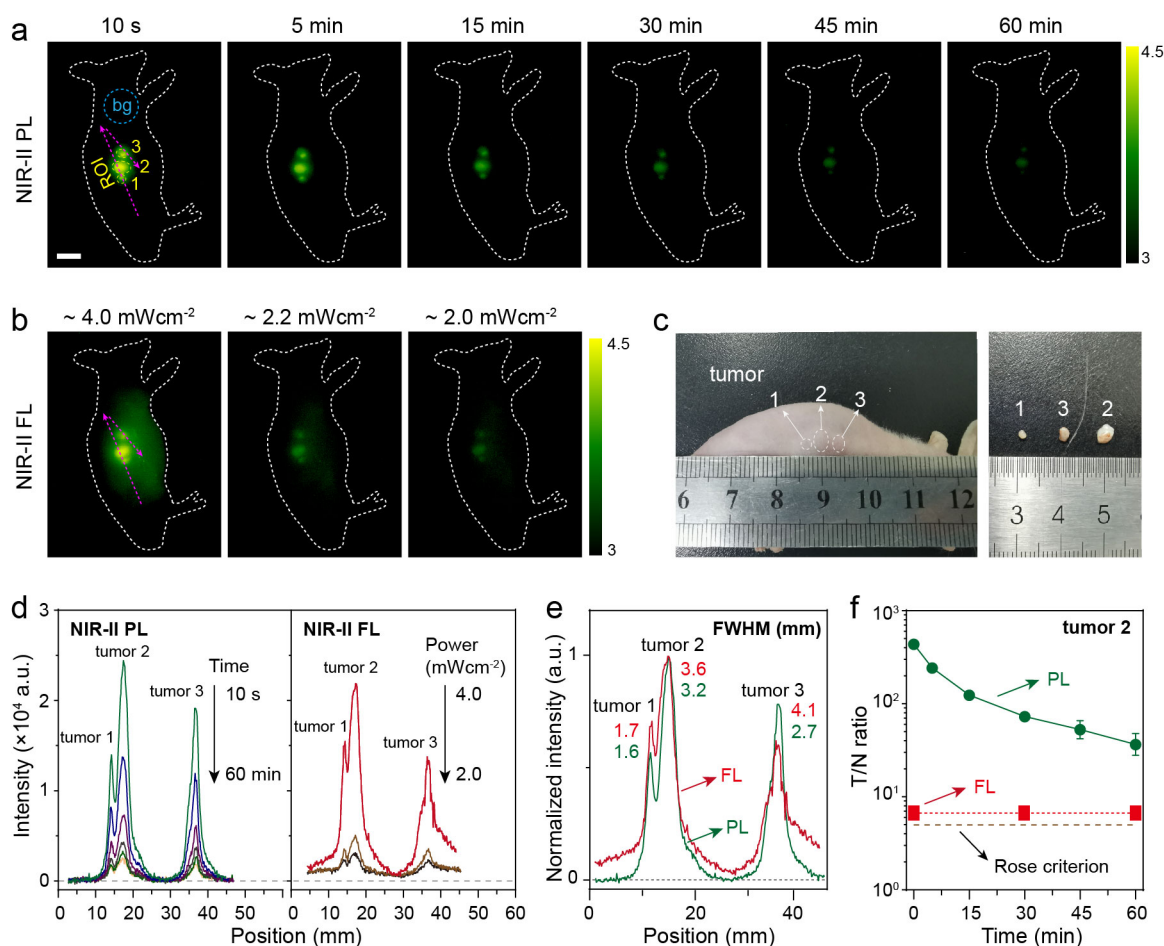
Extended Data Fig. 9 | *In vivo* NIR-II persistent luminescence and NIR-II fluorescence imaging of tumours using Nd-PLNPs (NaYF$_4$:1%Nd@NaYF$_4$).
a–c, NIR-II PL images (**a**), NIR-II FL images (**b**) and optical photos (**c**) of ultrasmall CT-26 tumours in a living mouse. **d**, Corresponding intensity profiles of NIR-II PL images in **a** and NIR-II FL images in **b** overtime. **e**, Normalized intensity profiles of NIR-II PL image (t = 10 s) and NIR-II FL image (808 nm laser power: 4 mWcm^{-2}). **f**, Tumour-to-normal tissue (T/N) ratios of the tumour 2 shown in **a** and **b** as a function of time (*n* = the number of pixels within the corresponding *ROI* in **a** and **b**). Scale bar: 1 cm. Imaging exposure time for PL and FL imaging is 10 s and 0.1 s, respectively. Nd-PLNPs were injected into ultra-small tumors (1.5–3.5 mm) of living mice. NIR-II PL imaging of tumour showed sharper FWHM (0.94-fold for tumour 1, 0.89-fold for tumour 2, and 0.66-fold for tumour 3) than that of NIR-II FL imaging due to reduced background noise without excitation light. Meanwhile, the tumour-to-normal tissue (T/N) ratio recorded from PL imaging reached 437.6 after injection for 10 s, which was ~ 65.3-fold higher than that of NIR-II FL (~ 6.7). Although the T/N ratios decreased with PL signal attenuation, they maintained above ~ 36 over 60 min, which was 7 times higher than the Rose criterion.
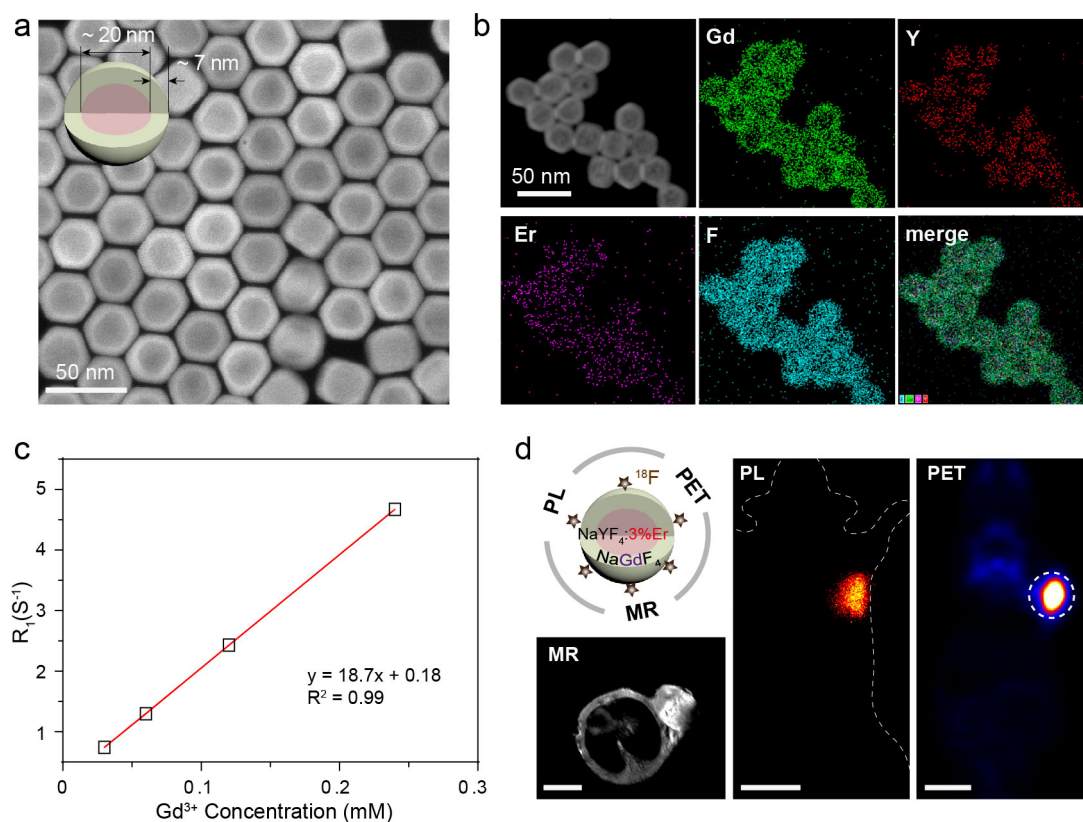
Extended Data Fig. 10 | Multimodal imaging of tumours in a living mouse using NaYF$_4$:3%Er@NaGdF$_4$-(^{18}F) probe. a, HAADF-STEM image of NaYF$_4$:3%Er@NaGdF$_4$ nanoparticles. **b**, Element mapping of NaYF$_4$:3%Er@NaGdF$_4$ nanoparticles. **c**, Relaxation rate R$_1$ (1/T$_1$) versus various Gd^{3+} concentrations of NaYF$_4$:3%Er@NaGdF$_4$ nanoparticles (0.03, 0.06, 0.12, and 0.24 mM) at room temperature. **d**, PL, MR and PET imaging of the tumour on a living mouse after intratumoural injection of NaYF$_4$:3%Er@NaGdF$_4$-(^{18}F) probe. Scale bar: 1 cm. This is the first investigation of combined PET, MRI and NIR-II PL signals into single nanoparticles for multimodal *in vivo* imaging of tumours. In comparison, conventional PL materials are mainly large crystals, which are grown at extremely high temperatures (> 1000 °C) and lack nanostructured modulation and designability, thus hampering advanced multimodal bioimaging and biosensing. Because the signals of PET and MRI are affected by ^{18}F and Gd^{3+}, respectively, similar performance to reported ^{18}F-labeled NaGdF$_4$-based probes can be obtained using our NaYF$_4$:3%Er@NaGdF$_4$-(^{18}F) PLNPs. The longitudinal proton relaxation rate (R$_1$) as a function of Gd^{3+} concentration in our NaYF$_4$:3%Er@NaGdF$_4$ led to a R$_1$ relaxivity of 18.7 mM^{-1}·s^{-1}, which is lower than that of NaGdF$_4$-based probes (28.39 mM^{-1}·s^{-1})[51] but is 5.4-fold higher than that of clinically used Gd-DTPA (3.45 mM^{-1}·s^{-1})[52].

nature research

Corresponding author(s):   Fan Zhang, Yanmin Yang, Fan Yong

Last updated by author(s):   Apr 26, 2021

Reporting Summary

Nature Research wishes to improve the reproducibility of the work that we publish. This form provides structure for consistency and transparency in reporting. For further information on Nature Research policies, see our Editorial Policies and the Editorial Policy Checklist.

Statistics

For all statistical analyses, confirm that the following items are present in the figure legend, table legend, main text, or Methods section.

n/a	Confirmed	
☐	☒	The exact sample size (*n*) for each experimental group/condition, given as a discrete number and unit of measurement
☐	☒	A statement on whether measurements were taken from distinct samples or whether the same sample was measured repeatedly
☒	☐	The statistical test(s) used AND whether they are one- or two-sided *Only common tests should be described solely by name; describe more complex techniques in the Methods section.*
☒	☐	A description of all covariates tested
☒	☐	A description of any assumptions or corrections, such as tests of normality and adjustment for multiple comparisons
☐	☒	A full description of the statistical parameters including central tendency (e.g. means) or other basic estimates (e.g. regression coefficient) AND variation (e.g. standard deviation) or associated estimates of uncertainty (e.g. confidence intervals)
☒	☐	For null hypothesis testing, the test statistic (e.g. *F*, *t*, *r*) with confidence intervals, effect sizes, degrees of freedom and *P* value noted *Give P values as exact values whenever suitable.*
☒	☐	For Bayesian analysis, information on the choice of priors and Markov chain Monte Carlo settings
☒	☐	For hierarchical and complex designs, identification of the appropriate level for tests and full reporting of outcomes
☒	☐	Estimates of effect sizes (e.g. Cohen's *d*, Pearson's *r*), indicating how they were calculated

Our web collection on statistics for biologists contains articles on many of the points above.

Software and code

Policy information about availability of computer code

Data collection	A LabVIEW program was used to control the NIR-II imaging system and acquire images.
Data analysis	Imaging analysis: MATLABR2015a, ImageJ; Data representation: originPro8, Graphpad 6.02, Adobe illustrator CS6;

For manuscripts utilizing custom algorithms or software that are central to the research but not yet described in published literature, software must be made available to editors and reviewers. We strongly encourage code deposition in a community repository (e.g. GitHub). See the Nature Research guidelines for submitting code & software for further information.

Data

Policy information about availability of data

All manuscripts must include a data availability statement. This statement should provide the following information, where applicable:

- Accession codes, unique identifiers, or web links for publicly available datasets
- A list of figures that have associated raw data
- A description of any restrictions on data availability

The data that support the plots within this paper and other findings of this study are available from the corresponding authors upon reasonable request.

Field-specific reporting

Please select the one below that is the best fit for your research. If you are not sure, read the appropriate sections before making your selection.

☒ Life sciences ☐ Behavioural & social sciences ☐ Ecological, evolutionary & environmental sciences

For a reference copy of the document with all sections, see nature.com/documents/nr-reporting-summary-flat.pdf

Life sciences study design

All studies must disclose on these points even when the disclosure is negative.

Sample size	No sample size calculations were performed. The sample size (n) of each experiment is provided in the corresponding figure captions in the paper and supplementary information. Sample sizes were chosen to support meaningful conclusions.
Data exclusions	No data were excluded from the analyses.
Replication	Animal experiments were performed on biological replicates following identical procedures to verify the reproducibility of the experimental findings.
Randomization	The mice used in experiments were randomly allocated into the positive and control groups.
Blinding	Investigators were not blinded to group allocation during data collection and analysis.

Reporting for specific materials, systems and methods

We require information from authors about some types of materials, experimental systems and methods used in many studies. Here, indicate whether each material, system or method listed is relevant to your study. If you are not sure if a list item applies to your research, read the appropriate section before selecting a response.

Materials & experimental systems

n/a	Involved in the study
☒	☐ Antibodies
☐	☒ Eukaryotic cell lines
☒	☐ Palaeontology and archaeology
☐	☒ Animals and other organisms
☒	☐ Human research participants
☒	☐ Clinical data
☒	☐ Dual use research of concern

Methods

n/a	Involved in the study
☒	☐ ChIP-seq
☒	☐ Flow cytometry
☒	☐ MRI-based neuroimaging

Eukaryotic cell lines

Policy information about cell lines

Cell line source(s)	HEK-293, CT-26 and 4T1 cell lines
Authentication	All cell lines were authenticated by Short Tandem Repeat test.
Mycoplasma contamination	All cell lines tested negative for mycoplasma contamination.
Commonly misidentified lines (See ICLAC register)	No commonly misidentified cell lines were used in the study.

Animals and other organisms

Policy information about studies involving animals; ARRIVE guidelines recommended for reporting animal research

Laboratory animals	BALB/c mice (6-8 weeks, female, with an average weight of 20g) and ICR mice (8-10 weeks, male, with an average weight of 30g) were obtained from Shanghai SLRC Laboratory Animal Centre
Wild animals	The study do not involved wild animals.
Field-collected samples	No filed-collected samples were used in the study.

Ethics oversight | All protocols for animal experiments were in strict accordance with the National Institutes of Health Guide for the Care and Use of Laboratory Animals, and approved by Animal Care and Use Committee of Fudan University.

Note that full information on the approval of the study protocol must also be provided in the manuscript.